

Pleistocene to recent evolution of Mocho-Choshuenco volcano during growth and retreat of the Patagonian Ice Sheet

Pablo Moreno-Yaeger^{1,†}, Brad S. Singer¹, Benjamin R. Edwards², Brian R. Jicha¹, William O. Nachlas¹, Mark D. Kurz³, Rachel E. Breunig¹, Ivo Fustos-Toribio⁴, Daniel Vásquez Antipán⁴, and Ella Piergrossi²

¹Department of Geoscience, University of Wisconsin-Madison, Madison, Wisconsin 53706, USA

ABSTRACT

(39.9°S, Mocho-Choshuenco volcano 72.0°W) produced \sim 75 explosive eruptions following retreat of the >1.5-km-thick Patagonian Ice Sheet associated with the local Last Glacial Maximum (LGM, from 35 to 18 ka). Here, we extend this record of volcanic evolution to include pre- and syn-LGM lavas that erupted during the Pleistocene. We establish a long-term chronology of magmatic and volcanic evolution and evaluate the relationship between volcanism and loading/unloading of the Patagonian Ice Sheet via twenty-four ⁴⁰Ar/³⁹Ar and two ³He age determinations integrated with stratigraphy and whole-rock compositions of lava flows and glass compositions of tephra. Our findings reveal that the edifice is much younger than previously thought and preserves 106 km³ of eruptive products, of which 50% were emplaced immediately following the end of the penultimate glaciation and 20% after the end of the LGM. A period of volcanic inactivity between 37 and 26 ka, when glaciers expanded, was followed by the eruption of incompatible element-rich basaltic andesites. Several of these syn-LGM lavas dated between 26 and 16 ka, which crop out at 1500-1700 m above sea level, show ice contact features that are consistent with emplacement against a 1400- to 1600-m-thick Patagonian Ice Sheet. Small volume dacitic eruptions and two explosive rhyolitic eruptions dominate the volcanic output from 18 to 8 ka, when the Patagonian Ice Sheet began to retreat rapidly. We hypothesize that increased lithostatic loading as the Patagonian

Pablo Moreno-Yaeger https://orcid.org/0000 -0001-5219-4546 †morenoyaeger@wisc.edu

Ice Sheet grew prohibited dike propagation, thus stalling the ascent of magma, promoting growth of at least three discrete magma reservoirs, and enhancing minor crustal assimilation to generate incompatible elementrich basaltic andesitic to dacitic magmas that erupted between 26 and 17 ka. From an adjacent reservoir, incompatible element-poor dacites erupted from 17 to 12 ka. These lava flows were followed by the caldera-forming eruption at 11.5 ka of 5.3 km³ of rhyolite from a deeper reservoir atop which a silicic melt lens had formed and expanded. Subsequent eruptions of oxidized dacitic magmas from the Choshuenco cone from 11.5 to 8 ka were followed by andesitic to dacitic eruptions at the more southerly Mocho cone, as well as small flank vent eruptions of basaltic andesite at 2.5 and 0.5 ka. This complex history reflects a multi-reservoir plumbing system beneath Mocho-Choshuenco, which is characterized by depths of magma storage, oxidation states, and trace element compositions that vary over short periods of time (<2 k.y.).

INTRODUCTION

The processes by which transcrustal magma plumbing systems are destabilized to promote potentially dangerous volcanic eruptions may be propelled by either internal or external forces (Cashman et al., 2017). Examples of internal forcing mechanisms include fractional crystallization to overcome neutral buoyancy, exsolution of volatiles that expands and lowers the density of magma, crustal assimilation, mingling and mixing of magmas, and dissolution of crystals (e.g., Pallister et al., 1992; Singer et al., 2016; Huber et al., 2019; Townsend and Huber, 2020; Caricchi et al., 2021; Townsend, 2022). Exter-

nal forcing can reflect seismically induced stress changes (Yokoyama, 1988; Hill et al., 2002; Manga, 2007; Avouris et al., 2017; Sawi and Manga, 2018; Caricchi et al., 2021), hydrothermal alteration (Cashman et al., 2017), sea-level rise and fall (Satow et al., 2021; Jicha et al., 2023), edifice failure via landslide or debris avalanche (McGuire, 1996; Hora et al., 2007; Gouhier and Paris, 2019; Belousov et al., 2020), and surface loading and unloading via growth and decay of ice sheets or glaciers (Edwards et al., 2002; Jellinek et al., 2004; Huybers and Langmuir, 2009; Watt et al., 2013; Rawson et al., 2016a).

Owing to the slow growth of the Patagonian Ice Sheet to >1.5 km in thickness (Davies et al., 2020; Cuzzone et al., 2024) between ca. 35 and 18 ka during the local Last Glacial Maximum (LGM; Denton et al., 1999) and its rapid retreat between 18 and 15 ka (Moreno et al., 2015; Alloway et al., 2022), it has been proposed that volcanoes within the Andean Southern Volcanic Zone are ideal candidates for investigating the role of ice sheet loading and unloading on magma plumbing systems (Watt et al., 2013). Particularly, the eruptive history of the Mocho-Choshuenco Volcanic Complex (here Mocho-Choshuenco) has been interpreted to reflect a strong response following deglaciation. Based on the post-LGM tephra record, Rawson et al. (2016a) proposed a model of changes in the eruptive rates and compositions of magmas in the transcrustal magma plumbing system beneath Mocho-Choshuenco volcano. Rawson et al.'s (2016a) three-phase model includes: large eruptions of long-stored, SiO2-rich magma from 13 to 8 ka (Phase 1), followed by refilling of the reservoir to produce small mafic eruptions from 7 to 3 ka (Phase 2), culminating in an uptick in rate and andesitic activity during the past 2.4 k.y. (Phase 3). The \sim 5 k.y. lag after the LGM

GSA Bulletin; published online 7 June 2024 https://doi.org/10.1130/B37514.1.

²Department of Geosciences, Dickinson College, Carlisle, Pennsylvania 17013, USA

³Woods Hole Oceanographic Institution, Woods Hole, Massachusetts 02543, USA

⁴Department of Civil Engineering, University of La Frontera, Temuco 4811230, Chile

could imply a slow relaxation of stress within the crust, reflecting a protracted viscoelastic response (Jellinek et al., 2004) or an incomplete post-LGM volcanic record owing to erosion or lack of preservation of tephra during the initial retreat of ice between 18 and 16 ka (Fontijn et al., 2014; Rawson et al., 2016a). Notably, this model is based solely on postglacial tephra and does not account for the effusive eruptions of lava flows that occurred throughout the history of Mocho-Choshuenco including prior to, during, and after the LGM.

Investigating the response of ice loading and unloading at continental arc volcanoes is challenging due to the potential biased preservation of the eruptive products and limited precision of geochronometers (Conway et al., 2023). However, advances in 40Ar/39Ar dating of Pleistocene to Holocene lava flows (e.g., Singer et al., 2008; Wijbrans et al., 2011; Andersen et al., 2017; Conway et al., 2018; Preece et al., 2018; Martínez et al., 2018; Mixon et al., 2021; Klug et al., 2022) and ³He surface exposure dating of Holocene lavas (e.g., Fenton and Niedermann, 2014; Parmelee et al., 2015) offer powerful means for extending beyond, and building upon, the radiocarbon-dated post-LGM tephra record to address the long-term evolution of large composite volcanoes. Establishing such longer term records for the growth of Andean Southern Volcanic Zone volcanoes is key to: (1) tracking changes, if any, in processes operating internally within the transcrustal plumbing system; (2) determining whether magma reservoirs of a particular composition are more susceptible to destabilization via glacial loading and unloading; (3) estimating cumulative eruptive volumes and changes in eruptive rate; (4) modeling erosion rates; and (5) better assessing future volcanic hazards. Moreover, dating lava-ice interactions at higher elevations on composite volcanoes can provide spatiotemporal constraints on the extent and thickness of glaciers and the enveloping ice sheet (e.g., Edwards et al., 2002; Conway et al., 2015; Smellie and Edwards, 2016; Mixon et al., 2021; Harris et al., 2023).

Here, we expand upon previous dating efforts at Mocho-Choshuenco (Moreno and Lara, 2007; Rawson et al., 2015) via twenty-four new ⁴⁰Ar/³⁹Ar and two ³He age determinations of pre-, syn- and post-LGM lavas and proximal tephras. Moreover, we correlate effusive products with tephras previously defined using glass chemistry and magnetite-ilmenite oxybarometry by Rawson et al. (2015). To constrain the evolution of the magma plumbing system through time and explore possible impacts of glacial loading and unloading, we couple the chronology with 113 whole-rock major and trace element compositions and more than 200 glass shard composi-

tions. Ice contact features suggest that syn-LGM lavas that erupted between 26 and 18 ka flowed against a 1400- to 1600-m-thick Patagonian Ice Sheet surrounding the edifice. Our results show that Mocho-Choshuenco is much younger than previously thought, with mafic eruptions occurring since the beginning of cone growth at ca. 300 ka into the recent (A.D. 1864), but also that silicic magmas erupted voluminously only between 18 and 8 ka, including an \sim 5 km³ rhyolitic tephra associated with the collapse of a 3.5-km-wide summit caldera at 11.5 ka. Contrasts in the oxidation state and major and trace element composition of magmas that erupted over a short period time (<2 k.y.) suggest a complex architecture within the magma plumbing system with multiple reservoirs, some of which were sensitive to ice loading and unloading, and others less so.

GEOLOGIC SETTING

Mocho-Choshuenco is a composite volcano covering 250 km², comprising 106 km³ at 39.9°S in the Los Ríos region of the Andean Southern Volcanic Zone of Chile, ~730 km south of Santiago (Fig. 1; SERNAGEOMIN, 2020), with potentially active vents <10 km from heavily visited tourist towns (Fig. 2). The Andean Southern Volcanic Zone reflects subduction of the Nazca plate beneath the South American plate at 7-9 cm/yr (Somoza, 1998; DeMets et al., 2010; Fig. 1). The 1200-km-long Liquiñe-Ofqui Fault System and Andean Transverse Faults have been interpreted to control the location and transport of magma beneath some of the composite volcanoes and several minor monogenetic cones in the Andean Southern Volcanic Zone (López-Escobar et al., 1995; Cembrano and Lara, 2009; Pérez-Flores et al., 2016; Hickey-Vargas et al., 2016).

Mocho-Choshuenco is located 10 km west of the Liquiñe-Ofqui Fault System and comprises the main NW-SE-aligned Mocho and Choshuenco edifices, as well as 40 minor eruptive centers on its flanks (Fig. 2). The current Mocho cone reaches an elevation of 2422 m above sea level (masl) and is capped by the Mocho glacier, both of which are primarily within an \sim 3.5-km-diameter caldera (Fig. 3) that is hypothesized to be younger than 60 ka in age by Moreno and Lara (2007). The Choshuenco edifice reaches 2415 masl. The volcanic complex overlies Paleozoic granitoids and metamorphic rocks (Moreno and Lara, 2007), which are locally intruded by Mesozoic granitoids that are, in turn, intruded and overlain by Miocene plutons and Oligocene-Miocene metasedimentary rocks, respectively (Di Biase, 1976; McMillan et al., 1989; Rodríguez et al., 1999; Moreno and Lara, 2007). The northern Patagonian region has been impacted by at least two major glacial-deglacial cycles during the past 150 k.y. These include: (1) the transition from the penultimate glaciation of marine isotope stage (MIS) 6 between 191 and 130 ka into the interglacial period of MIS 5 from 130 to 80 ka, and (2) the local LGM between ca. 35 and 18 ka and the post-LGM deglaciation that was nearly complete by 15 ka (Moreno et al., 2015; Alloway et al., 2022; Cuzzone et al., 2024). Although evidence supporting an advance of the Patagonian Ice Sheet during MIS 4 between ca. 71 and 57 ka has been discovered farther south along the Strait of Magellan (Peltier et al., 2021), it remains unclear how significant this advance might have been in northern Patagonia, including at Mocho-Choshuenco volcano.

The eruptive history of Mocho-Choshuenco has traditionally been subdivided into eight units (Mocho 1, 2, 3, 4, and 5; Choshuenco 1 and 2; and the Secuencia Piroclástica units; Moreno and Lara, 2007). The eleven 40Ar/39Ar ages reported by Moreno and Lara (2007) have relatively large uncertainties, and the supporting isotopic data and laboratory procedures are not reported, which makes it difficult to evaluate the accuracy of their chronostratigraphy. Moreno and Lara (2007) suggest that cone growth began with basaltic andesitic to andesitic lavas from 350 to 100 ka (Mocho 1 and 2 and Choshuenco 1 units), followed by andesitic to dacitic lavas from 100 ka to the present (Mocho 3, 4, and 5, and Choshuenco 2 units). The Secuencia Piroclástica (Pyroclastic Sequence) comprises ~75 post-LGM tephras that range in composition from basaltic andesite to rhyolite (52–73 wt% SiO₂; Rawson et al., 2015; Table 1). The most voluminous eruption is the 5.3 km³ Neltume rhyolite (11.5 ka), which accounts for 27% of the total post-LGM eruptive volume. Alloway et al. (2022) recently identified the MC2 tephra (Rawson et al., 2015) 85 km south of Mocho-Choshuenco, which suggests that this rhyolitic eruption was larger than previously estimated.

Holocene eruptive products on the flanks of Mocho-Choshuenco include the basaltic andesitic to andesitic (53.4–60.8 wt% SiO₂) Alto Caunahue and Ranquil cones (Fig. 2). The Grupo Fui and Volcanes Chanchán are a series of monogenetic cones located on the far northeastern flank of Mocho-Choshuenco (Moreno and Lara, 2007; Gardeweg and Sellés, 2012; Rawson et al., 2016b; Fig. 2). They have erupted magmas that are compositionally distinct from calc-alkaline Mocho-Choshuenco products (Rawson et al., 2016b; Mallea-Lillo et al., 2022). These monogenetic eruptions likely exploit the Liquiñe-Ofqui Fault System as a conduit and thus are not associated with the magma plumbing system beneath

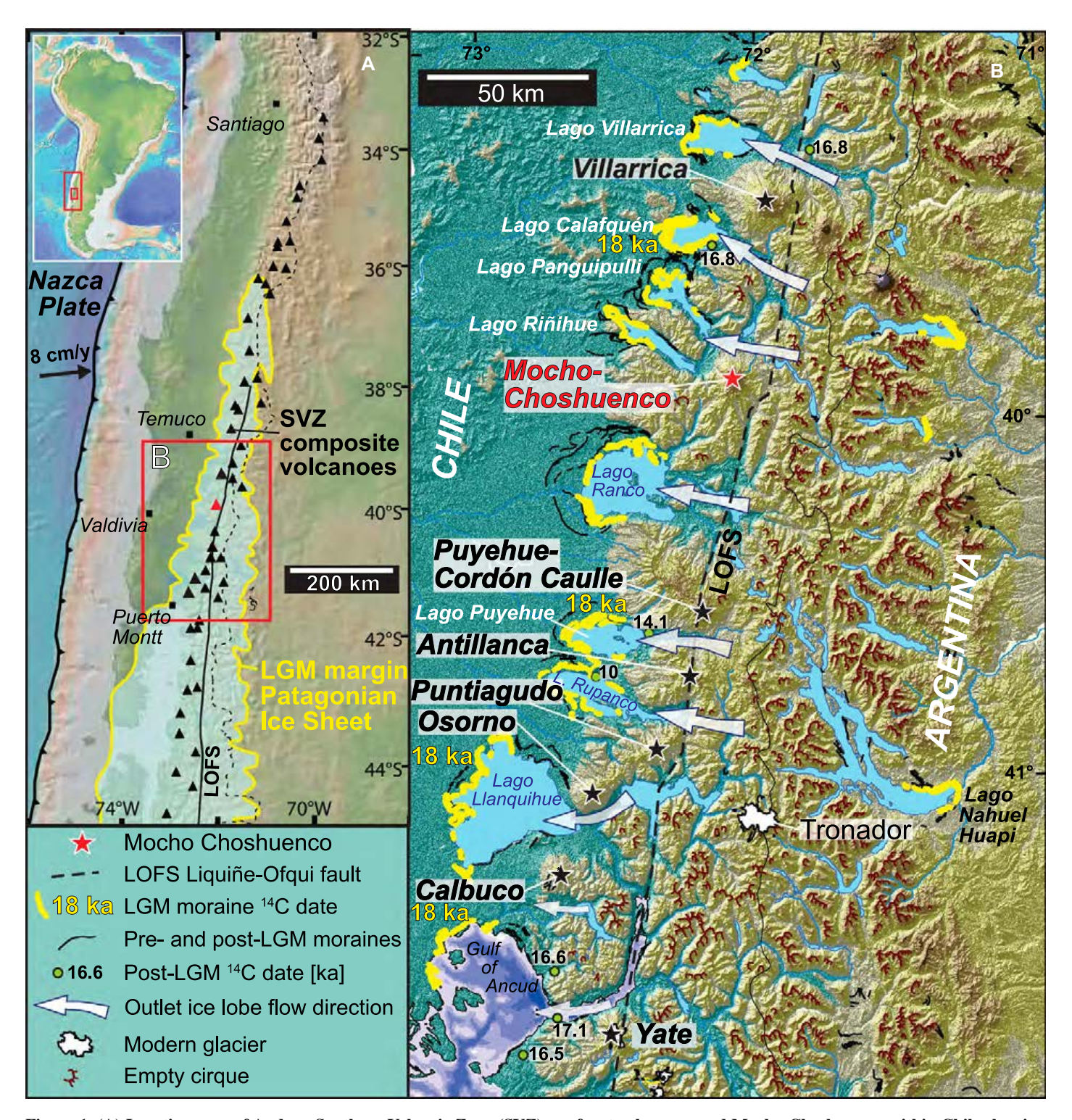


Figure 1. (A) Location map of Andean Southern Volcanic Zone (SVZ) arc front volcanoes, and Mocho-Choshuenco, within Chile showing margin of the Patagonian Ice Sheet at the Last Glacial Maximum (LGM, 18 ka). (B) Enlargement of red box in panel A. Yellow lines: moraines deposited between 23 and 17.8 ka, which impound large proglacial lakes; those marked 18 ka are associated with many ¹⁴C dates. Black stars indicate locations of frontal arc volcanoes: Villarrica, Puyehue-Cordón Caulle (here we refer only to Puyehue stratocone), Antillanca, Mocho-Choshuenco, Calbuco, and Osorno. White arrows indicate major outlet glacial lobes of the Patagonian Ice Sheet, which followed throughgoing valleys (panel B is modified from Davies et al., 2020).

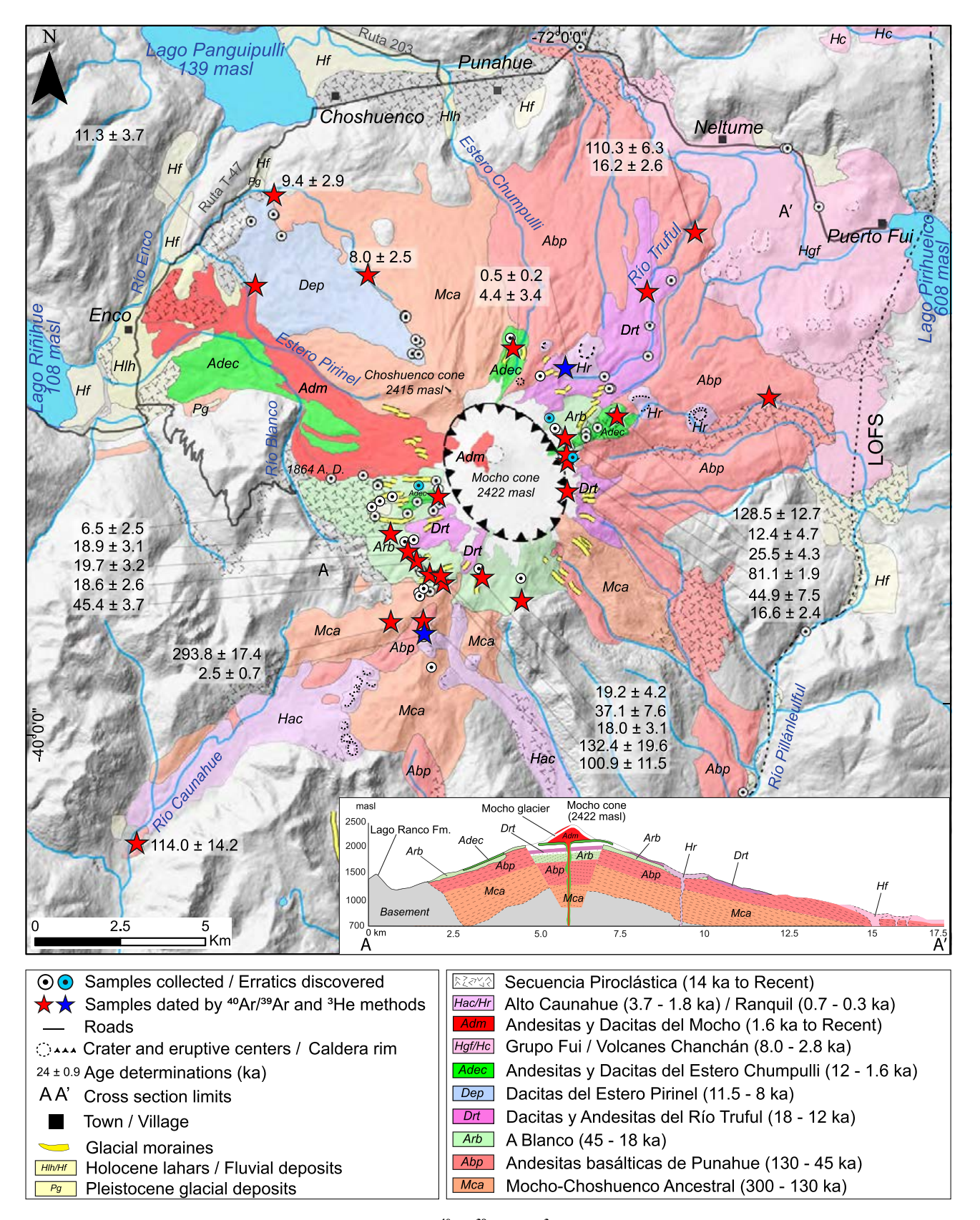


Figure 2. Geologic map of Mocho-Choshuenco based on ⁴⁰Ar/³⁹Ar and ³He age determinations shown in red and blue stars, respectively. Samples of Neltume tephra were collected more than 30 km north of the main cone, outside of the area shown in this map. Liquine Ofqui Fault System (LOFS) denoted by dashed line to the east of Mocho-Choshuenco.

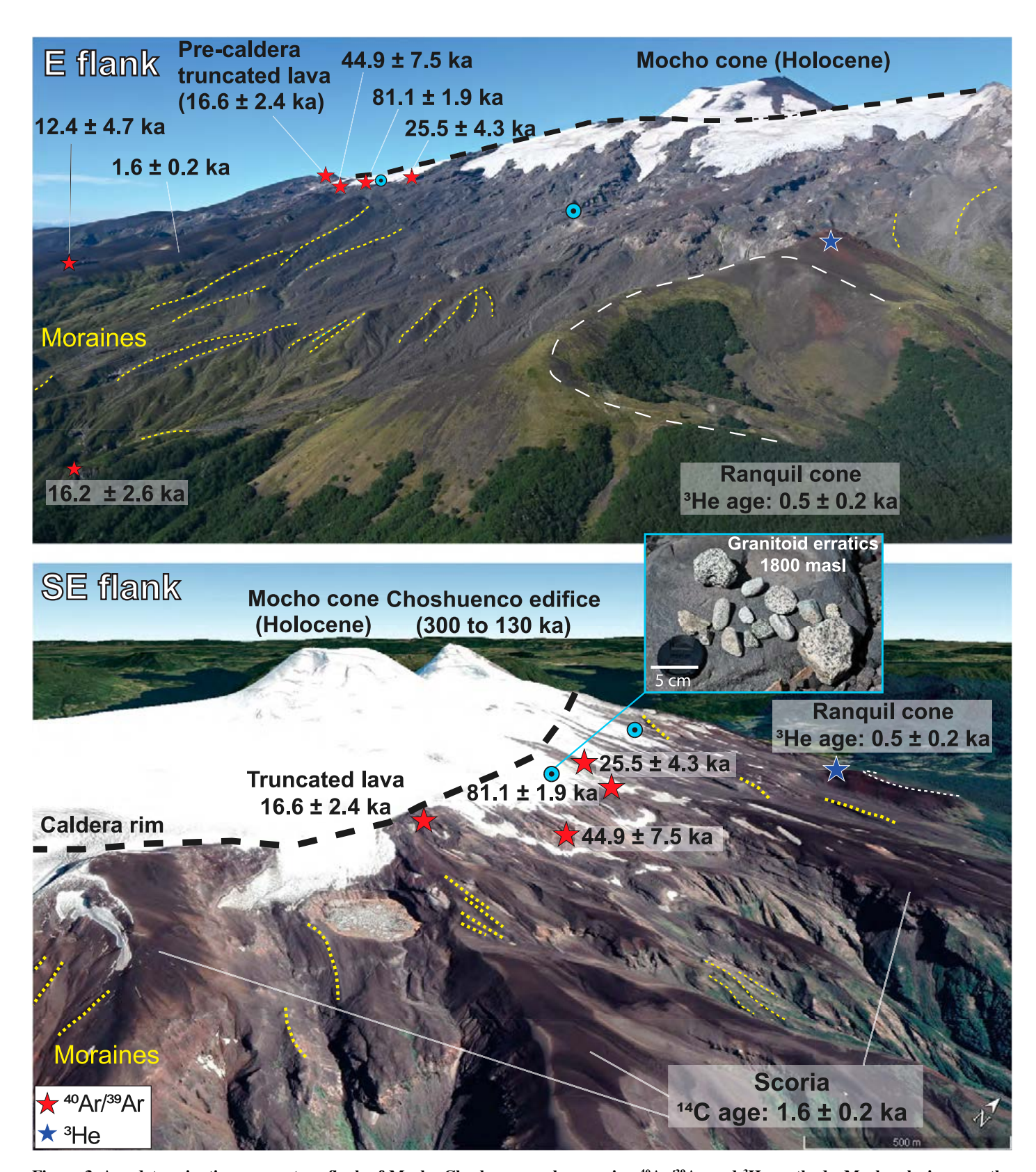


Figure 3. Age determinations on eastern flank of Mocho-Choshuenco volcano using ⁴⁰Ar/³⁹Ar and ³He methods. Mocho glacier caps the edifice. Upper panel photo was taken from helicopter, and lower panel is a Google Earth base map. Dashed yellow lines are lateral moraine crests. Dashed white lines represent the Ranquil cone crater. Scoria represents Enco ignimbrite dated at 1.6 ka by Rawson et al. (2015). Light blue box indicates granitoid erratics found in the area (Fig. 2).

TABLE 1. SUMMARY OF 40Ar/39Ar AGE DETERMINATIONS OF MOCHO-CHOSHUENCO LAVAS

| Sample | Мар | # exp. | SiO ₂ (wt%) | Latitude (°S) | Longitude (°W) | Altitude (masl) | Isochron | | | Plateau | | | |
|-----------|------|-----------|---------------------------|------------------|-------------------|--------------------|------------------------------------|------|---|---------|------|-------------------------|------------------------------------|
| | unit | | | | | | Age (ka) \pm 2 σ | MSWD | $(^{40}$ Ar/ 36 Ar) $_{i}$ $\pm 2\sigma$ | N | MSWD | ³⁹ Ar (%) | Age (ka) \pm 2 σ |
| MC-22-28 | Adec | 2 | 56.1 | 39.9027 | 72.0196 | 1579 | 2.0 ± 2.8 | 0.45 | 299.1 ± 1.5 | 26/30 | 1.19 | 75 | 4.4 ± 3.4 |
| MC-20-19 | Adec | 2 | 63.6 | 39.9420 | 72.0545 | 1846 | $\textbf{6.1} \pm \textbf{2.4}$ | 0.49 | 298.4 ± 0.9 | 29/33 | 0.31 | 94 | 6.5 ± 2.5 |
| MC-20-34 | Dep | 3 | 66.6 | 39.8928 | 72.0566 | 1366 | $\textbf{4.2} \pm \textbf{2.1}$ | 0.41 | 300.1 ± 1.1 | 44/50 | 0.58 | 99 | 8.0 ± 2.5 |
| MC-20-48 | Dep | 2 | 64.8 | 39.8601 | 72.0998 | 316 | 11.2 \pm 7.1 | 0.40 | 298.2 ± 3.7 | 18/27 | 1.10 | 87 | $\textbf{9.4} \pm \textbf{2.9}$ |
| MC-20-50 | Dep | 2 | 63.0 | 39.8833 | 72.1073 | 363 | $\textbf{8.4} \pm \textbf{3.7}$ | 0.03 | 299.3 ± 2.4 | 28/28 | 1.70 | 100 | $\textbf{11.3} \pm \textbf{3.7}$ |
| MC-22-09 | Adec | 2 | 52.5 | 39.9219 | 71.9844 | 1445 | 7.7 ± 3.5 | 1.80 | 299.1 ± 1.3 | 29/29 | 0.57 | 100 | $\textbf{12.4} \pm \textbf{4.7}$ |
| MC-20-04B | Drt | 4 | 61.4 | 39.9139 | 71.9874 | 1282 | $\textbf{16.7} \pm \textbf{4.4}$ | 0.76 | 298.4 ± 0.7 | 54/59 | 0.94 | 99 | $\textbf{16.2} \pm \textbf{2.6}$ |
| MC-22-18 | Drt | 2 | 64.2 | 39.9409 | 72.0024 | 1907 | $\textbf{19.8} \pm \textbf{4.6}$ | 0.75 | 297.0 ± 2.3 | 23/23 | 0.53 | 100 | $\textbf{16.6} \pm \textbf{2.4}$ |
| MC-20-61 | Arb | 2 | 52.5 | 39.9219 | 71.9844 | 1695 | 14.6 ± 4.7 | 1.22 | 299.4 ± 1.6 | 25/27 | 0.49 | 98 | $\textbf{18.0} \pm \textbf{3.1}$ |
| MC-20-25 | Arb | 1 | 54.9 | 39.9585 | 72.0551 | 1563 | $\textbf{21.4} \pm \textbf{7.0}$ | 0.86 | 297.9 ± 2.0 | 14/14 | 0.77 | 100 | $\textbf{18.6} \pm \textbf{2.6}$ |
| MC-20-28 | Arb | 3 | 53.9 | 39.9505 | 72.0638 | 1418 | 18.9 ± 7.5 | 1.90 | 297.7 ± 3.0 | 30/35 | 0.20 | 91 | $\textbf{18.9} \pm \textbf{3.1}$ |
| MC-22-15 | Arb | 2 | 54.0 | 39.9633 | 72.0195 | 1764 | 17.2 ± 11.6 | 0.00 | 299.8 ± 4.9 | 14/14 | 1.30 | 100 | $\textbf{19.2} \pm \textbf{4.4}$ |
| MC-20-27 | Drt | 1 | 63.8 | 39.9550 | 72.0581 | 1494 | $\textbf{25.9} \pm \textbf{9.4}$ | 0.91 | 297.7 ± 1.5 | 10/13 | 0.74 | 93 | 19.7 ± 3.2 |
| MC-20-40 | Arb | 1 | 52.6 | 39.9318 | 72.0018 | 1794 | 24.2 ± 9.3 | 1.27 | 298.7 ± 1.3 | 14/14 | 1.03 | 100 | 25.5 ± 4.3 |
| MC-22-21 | Arb | 1 | 53.5 | 39.9604 | 72.0338 | 1735 | $\textbf{36.2} \pm \textbf{11.2}$ | 1.31 | 298.6 ± 0.6 | 10/13 | 0.97 | 95 | 37.1 ± 7.6 |
| MC-20-39 | Arb | 2 | 57.8 | 39.9312 | 72.0016 | 1796 | 52.3 ± 15.8 | 0.38 | 297.1 ± 3.2 | 24/30 | 0.40 | 92 | 44.9 ± 7.5 |
| MC-20-59 | Arb | 3 | 55.9 | 39.9617 | 72.0508 | 1617 | 40.0 ± 11.8 | 2.30 | 299.2 ± 2.3 | 36/42 | 1.70 | 97 | $\textbf{45.4} \pm \textbf{3.7}$ |
| MC-20-38 | Abp | 2 | 66.6 | 39.9318 | 72.0018 | 1802 | 83.5 ± 4.7 | 1.75 | 297.9 ± 1.8 | 31/33 | 1.28 | 99 | 81.1 \pm 1.9 |
| MC-20-62 | Abp | 2 | 53.0 | 39.9659 | 72.0512 | 1660 | 59.3 ± 23.3 | 1.60 | 299.7 ± 3.4 | 33/34 | 0.57 | 100 | 100.9 ± 11.5 |
| MC-20-03 | Abp | 2 | 54.3 | 39.8738 | 71.9562 | 723 | $\textbf{109.4} \pm \textbf{6.2}$ | 0.67 | 299.5 ± 1.2 | 21/25 | 0.57 | 83 | $\textbf{110.3} \pm \textbf{6.3}$ |
| MC-20-01 | Abp | 2 | 52.5 | 40.0300 | 72.1545 | 439 | $\textbf{68.7} \pm \textbf{35.2}$ | 0.06 | $\textbf{301.4} \pm \textbf{2.2}$ | 27/30 | 0.48 | 96 | $\textbf{114.2} \pm \textbf{14.2}$ |
| MC-20-54C | Abp | 3 | 52.6 | 39.9176 | 71.9322 | 909 | $\textbf{163.4} \pm \textbf{27.5}$ | 0.54 | 294.7 ± 1.3 | 45/49 | 0.57 | 95 | 128.5 ± 12.7 |
| MC-20-60 | Mca | 2 | 55.0 | 39.9623 | 72.0468 | 1689 | $\textbf{94.8} \pm \textbf{22.1}$ | 0.74 | $\textbf{300.8} \pm \textbf{2.0}$ | 26/26 | 0.14 | 100 | $\textbf{132.4} \pm \textbf{19.6}$ |
| MC-22-29 | Mca | 1 | 55.9 | 39.9663 | 72.0547 | 1672 | $\textbf{298.9} \pm \textbf{23.4}$ | 1.00 | 299.3 ± 1.1 | 27/27 | 1.00 | 100 | 293.8 ± 17.4 |

Note: Ages relative to 1.1864 Ma Alder Creek sanidine (Jicha et al., 2016) using a total 40K decay constant of 5.463 ± 0.107 × 10⁻¹⁰ yr⁻¹ (Min et al., 2000). Atmospheric 40Ar/86Ar = 298.56 ± 0.31 (Lee et al., 2006). masl—meters above sea level; MSWD—mean square weighted deviation; Adec—Andesitas y dacitas del Estero Chumpulli; Dep—Dacitas del Estero Pirinel; Drt—Dacitas y andesitas del Río Truful; Arb—Andesitas basálticas del Río Blanco; Abp—Andesitas basálticas de Punahue; Mca—Mocho-Choshuenco Ancestral.

the Mocho-Choshuenco edifice (Moreno and Lara, 2007; Gardeweg and Sellés, 2012; Rawson et al., 2016b; Mallea-Lillo et al., 2022).

METHODS

Whole-Rock Major and Trace Element Composition

A total of 113 lava and tephra samples were collected during field campaigns between 2020 and 2022 (Fig. 2). Major and trace element compositions were obtained by X-ray fluorescence (XRF) and inductively coupled plasma-mass spectrometry (ICP-MS), respectively, at Hamilton Analytical Labs, Clinton, New York, USA. Samples were powdered in an alumina ring mill and weighed with Li-tetraborate in a proportion of one part powder to two parts flux, blended using a vortex mixer, and fused in graphite crucibles at 1000 °C. The fused pellets were cleaned of residual carbon, reground, refused at 1000 °C, and lapped flat in four stages with gradually finer diamond laps to a 15 µm finished surface. Loss on ignition (LOI) was measured by heating samples overnight in silica crucibles at 900 °C. The XRF measurements used a Thermo Scientific ARL PERFORM'X spectrometer operating at 45 kV accelerating voltage and 45 mA current. The system is recalibrated at 10-month intervals using ~70 certified reference standards. Drift was monitored with in-house standards AGV-1,

BHVO-1, and RGM-1 (Table S1¹), with uncertainties estimated to be better than $\pm 0.2\%$ (1 σ).

ICP-MS measurements followed Conrey et al. (2023). Samples and glass standards were ablated using a Photon Machines Analyte 193 (G1) ablation station (193 nm wavelength excimer laser with laminar flow cell) and carried into a Varian 820 ICP-MS using He gas with Ar gas in a mixing volume of 20 ml just before the torch. Drift was corrected by measuring an in-house monitor calibrated using 18 certified reference materials. For the elements of greatest interest, the relative uncertainty was $\pm 3\%$ –5%.

Glass Shard Compositions

The major and minor element composition of glass shards from seven post-LGM tephra samples was measured using a Cameca SX-Five field emission–electron probe microanalyzer at the University of Wisconsin–Madison Department of Geoscience, Madison, Wisconsin, USA. Grain mounts were polished to 1 µm surface finish and coated with 1 nm of Ir. Measurements were performed at 15 kV with beam current of 6 nA and defocused beam size of 5 or 10 µm.

Peaking and calibration were performed using natural and synthetic standards (Table S2). Accuracy of calibrations was evaluated from analysis of Smithsonian (Jarosewich et al., 1980) and MPI-DING (Jochum et al., 2006) glass reference materials (Table S3). Background subtraction was performed using a mean atomic number correction (Donovan et al., 2016) for major elements (Na, K, Al, Si, Mg, Ca, and Fe) and traditional off-peak regression for low-abundance elements (Mn, Ti, P, and Cl). A time-dependent intensity correction with exponential fit was applied to account for migration of Na, Si, and K.

40Ar/39Ar Geochronology

Groundmass from 50 lava flow samples was packaged in aluminum foil, loaded into 2.5-cm-diameter disks, and irradiated for two hours in the Cadmium-Lined In-Core Irradiation Tube reactor at the Oregon State University, Corvallis, Oregon, USA. J values were interpolated across each disk by using the measured ⁴⁰Ar*/³⁹Ar_K ratio of the 1.1864 Ma Alder Creek sanidine standard crystals (Jicha et al., 2016) that were placed in four to five positions within each disk.

Incremental heating experiments were conducted at the University of Wisconsin–Madison WiscAr Laboratory by degassing ~ 30 mg subsamples in 8–28 steps using a 55 W CO₂ laser. Measurements were conducted on a Noblesse 5-collector mass spectrometer (Jicha et al., 2016)

¹Supplemental Material. Figures S1–S3 and Tables S1–S5. Please visit https://doi.org/10.1130 /GSAB.S.25800166 to access the supplemental material; contact editing@geosociety.org with any questions.

and on an NGX 600 mass spectrometer following procedures in Mixon et al. (2022). The samples dated represent each map unit except Choshuenco 1 (350–200 ka), which consists of steep, inaccessible outcrops; Mocho 5 (post-1.6 ka; Moreno and Lara, 2007); and the post-LGM tephras that were $^{14}\mathrm{C}$ dated by Rawson et al. (2015). For samples that yielded initial 2σ uncertainties of >25%, replicate incremental heating experiments were conducted to improve the precision.

³He Geochronology

Two pristine, uneroded bombs that display a bread-crust surface texture were collected from the highest elevations on the rims of scoria cones from the Alto Caunahue and Ranquil units on the northeastern and southern flanks of Mocho-Choshuenco, respectively (Fig. 2). Topographic shielding of the samples was <5%, and locations and elevations were determined by GPS with uncertainties of ± 5 m. Olivine crystals of 250-710 µm in size were separated by hand picking from the uppermost 5 cm of each bomb. Helium measurements were performed at Woods Hole Oceanographic Institution using a fully automated noble gas mass spectrometer (MAP-215-50) with cryogenic separation of helium, neon, and argon. The mineral separates were first measured by crushing extraction in vacuum; the resulting olivine powder was then loaded into a copper foil boat and melted in a double vacuum resistance furnace using procedures described in Kurz (1986) and Kurz et al. (2014). Procedural furnace 4He blanks were run before and after each sample and were $8 \pm 1 \times 10^{-12}$ cc standard temperature and pressure, and required small blank corrections (<11%).

Cone Growth and Erosion Rates

Volumes of map units were calculated by measuring areas in GIS and estimating thicknesses based on field observations and drone imagery. Uncertainties in the rate of cone growth come from both the precision of the age determinations and the spatial ALOS PALSAR 12 m resolution (ASF DAAC, 2022) digital elevation model (DEM). Volume estimates were based on eroded products and hence minimal. We accounted for erosion by reconstructing pre-incision topography within extant incised valleys and applying stratigraphic principles and observations to extrapolate the timing of incision onset. First, we identified incised valleys-those that form from advective processes like fluvial and glacial erosion-on a 30-m-resolution DEM of Mocho-Choshuenco (NASA Shuttle Radar Topography Mission, 2013). We focused our analysis on 10 of 12 radial valleys that have incised through lava flows for

which 40Ar/39Ar ages have been obtained or ages can be inferred from stratigraphic relations (Fig. S1). In doing so, we avoided assumptions about changes in the extent of lava deposits that are not justified from modern morphology (Fig. S1). Following the methods of Ferrier et al. (2013), and outlined here, we mapped minimally eroded surfaces of the valley rim and fit a natural cubic spline to the rim to represent the topography within the valley pre-incision. We then subtracted the modern land surface elevation (extracted from the DEM) from the pre-incision surface elevations and employed the eruption ages presented in this work to constrain the time since the initiation of incision of a valley by considering the last incised lava unit (Fig. S2). Dividing the volume eroded out of each valley by its incisional age yields the average rate of erosion for that valley in volume/ time (V/t). By using this method, we quantified the minimum volume of lava eroded from Mocho-Choshuenco that is consistent with the modern topography and lava distribution. It is possible that some lava deposits have eroded along their long-axis extent, that some valleys previously incised have been completely infilled by more recent lava deposits, and that the modern valley rims used to reconstruct the pre-incision surfaces may also represent an eroded state. All of these scenarios would result in the erosion of larger volumes of lava than is represented by the minimum eroded volume estimates presented here.

RESULTS

⁴⁰Ar/³⁹Ar and ³He Age Determinations

Twenty-four out of 50 samples (48%) yielded ⁴⁰Ar/³⁹Ar plateau ages defined by 71%–100% of the gas released in 8-28 steps (Table 1; Fig. 4). The remaining samples gave discordant spectra that do not meet plateau criteria (Schaen et al., 2021), or they do not contain detectable radiogenic Ar (40Ar*) (Table S4, 40Ar/39Ar metadata). Because no evidence of excess argon is observed in the inverse isochron regressions, we used the plateau ages to infer time since eruption (Table 1; Fig. 4). Based on the new age determinations and stratigraphic positions, we suggest that lava flows with no detectable 40Ar* likely erupted during the past 5 k.y. ³He surface exposure ages of the two bombs indicate that eruptions from the Alto Caunahue and Ranquil cones took place at ca. 2.5 and 0.5 ka, respectively (Table 2), in agreement with their stratigraphic positions atop groups of lava flows that yield much older ages (Figs. 2 and 3).

Volcanic Stratigraphy

Building from Moreno and Lara (2007; Table S5), we revised map units for Mocho-

Choshuenco based on new stratigraphic observations, rock compositions, and geochronology, and followed the international stratigraphic code by using geographic locations for unit names (Murphy and Salvador, 1999). Our map units (Table 3) include: (1) Mocho-Choshuenco Ancestral (Mca, 300-130 ka; it comprises the previous Mocho 1 and Choshuenco 1 units), (2) Andesitas basálticas de Punahue (Abp, 130-45 ka; flows terminate close to the town of Punahue and comprise the previous Mocho 2 and 3 units), (3) Andesitas basálticas del Río Blanco (Arb, 45-18 ka; incised by the Blanco River, Arb comprises the previous Mocho 3 unit), (4) Dacitas y Andesitas del Río Truful (Drt, 18-12 ka; incised by the Truful River, Drt comprises the previous Mocho 4 unit), (5) Andesitas del Estero Pirinel (Dep, 11.5-8 ka; incised by Pirinel Creek, Dep comprises the previous Choshuenco 2 unit), (6) Andesitas y Dacitas del Estero Chumpulli (Adec, 12-1.6 ka; incised by Chumpulli Creek, Adec encompasses the previous Mocho 4 unit), and (7) Andesitas y Dacitas del Mocho (Adm, 1.6 ka to recent; the youngest unit from the Mocho cone, Adm comprises the previous Mocho 4 and 5 units). The Secuencia Piroclástica comprises tephra deposits from ~75 post-LGM explosive eruptions (Rawson et al., 2015) and two units comprising minor eruptive centers erupting in the flanks of the edifice (Alto Caunahue and Ranquil).

Most of the Mocho-Choshuenco edifice comprises lavas of varying thicknesses and a range of jointing characteristics (Table 3). Lavas older than 45 ka are characterized by typical columnar jointing with diameters of 1–2 m and generally with vertical orientations. Starting at 45 ka, lava thicknesses are more distinctly varied, as are the orientations and decimeter-scale sizes of columnar joints. Moreover, these lavas locally exhibit pervasive platy jointing and form finger-like ridges on lower flanks.

Major and Trace Element Compositions

The compositions of lava, tephra, and glass shards range from basaltic andesitic to rhyolitic (52.0–69.3 wt% SiO₂ based on anhydrous composition; Fig. 5; Tables S1–S3) and define a calc-alkaline trend. Lavas from Mocho and Choshuenco edifices show similar trends, with increasing SiO₂, K₂O, and Na₂O and decreasing Al₂O₃, MgO, and CaO. K₂O ranges from 0.6 to 2.1 wt%, and TiO₂ increases from 52 to 57 wt% SiO₂ and decreases from 57.0 and 67.5 wt% SiO₂. Some of the more SiO₂-poor lavas (<53 wt% SiO₂) possess MgO contents that vary by up to 2.3 wt% at a given SiO₂ content (Fig. 5).

Trace element compositions (Fig. 6) of the products of both the Mocho and Choshuenco

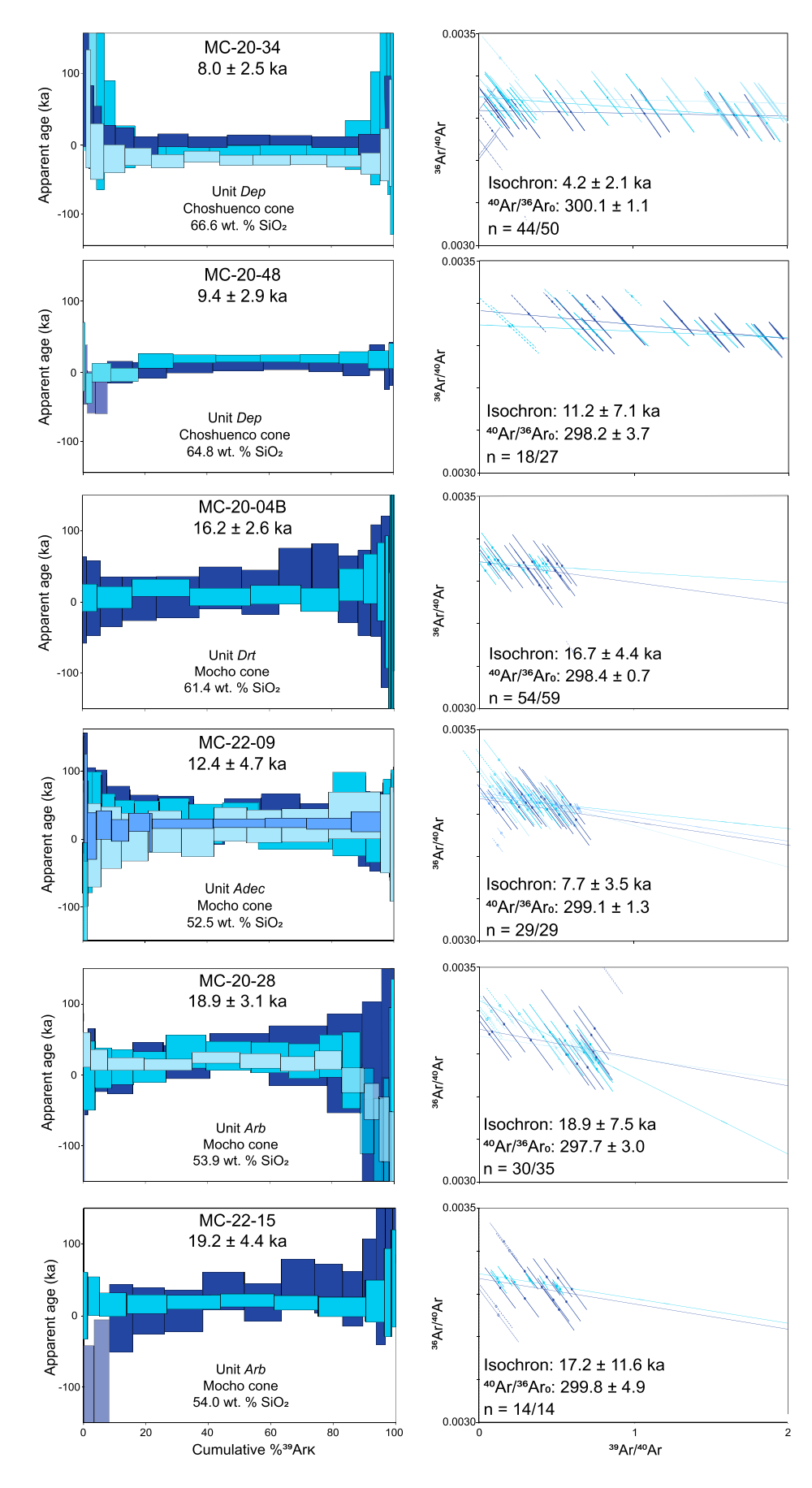


Figure 4. 40 Ar/ 39 Ar age spectrum and inverse isochrons from late Pleistocene and Holocene basaltic andesites and dacites that contain between 0.8 and 1.6 wt% K_2O . Uncertainties are reported as $\pm 2\sigma$ analytical. Each color reflects different experiments on the same sample.

edifices are broadly similar. However, distinct trends include one with relatively low incompatible element abundances (e.g., Th from 1 to 4 ppm, Zr from 50 to 150 ppm, and Rb from 10 to 40 ppm) and another with higher abundances (Th from 2 to 7 ppm, Zr from 100 to 300 ppm, and Rb from 18 to 60 ppm). Moreover, incompatible elements such as Zr and La range from 50 to 125 ppm and 5 to 15 ppm, respectively, in basaltic andesites with similar SiO₂ content (Fig. 6).

DISCUSSION

Eruptive Chronology

Here we integrate ⁴⁰Ar/³⁹Ar and ³He age determinations with whole-rock compositions to characterize each of the 10 mapped units in Figure 2 and Table 1.

Mocho-Choshuenco Ancestral (Mca; 300–130 ka)

Unit Mca comprises the oldest part of Mocho-Choshuenco—upon which the modern Mocho cone was built-and the highly eroded Choshuenco edifice on the northern flank (Fig. 2). Volcanic products are pyroxene- and olivine-bearing lavas and tephras intruded by a network of centimeter- to meter-thick feeder dikes, and volcanoclastic rocks on the southern flank. Magma compositions are basaltic andesitic to andesitic (52.1–61.2 wt% SiO₂), with minor dacitic flows (64.4 wt% SiO₂; Fig. 5). On the southern flank, lavas directly overlie the Oligo-Miocene basement (Lago Ranco Formation; Rodríguez et al., 1999; Fig. 2) at an elevation of 1500 masl and dip 5°-10°SW, whereas on the northern flank, they dip $\sim 30^{\circ}$ NE (Choshuenco edifice). The oldest dated lava flow on Mocho-Choshuenco is 293.8 ± 17.4 ka. Another flow dated at 132.4 ± 19.6 ka (Fig. 2) overlies feeder dikes exposed by repeated deep glacial erosion during the penultimate glaciation and LGM. Although we were unable to collect samples from the oldest lavas of the Choshuenco edifice, we consider these outcrops as part of Mca based on deep U-shaped valleys that expose a similar network of dikes on the northern flank of the edifice (Fig. 7). Based on these relation-

TABLE 2. SUMMARY OF ³He SURFACE EXPOSURE AGE DETERMINATIONS

| Summary data | MC-22-12 | MC-22-25 | | | | |
|--|---|---|--|--|--|--|
| Mapped unit | Ranquil (Hr) | Alto Caunahue (Hac) | | | | |
| Latitude (°S) | 39.9081 | 39.9714 | | | | |
| Longitude (°W) | 72.0015 | 72.0533 | | | | |
| Density (g/cm ³) | 2.8 | 2.9 | | | | |
| Altitude (masl) | 1605 | 1530 | | | | |
| Thickness (cm) | 5 | 4 | | | | |
| Shielding | 0.980 | 0.960 | | | | |
| Mass (g) | 0.33446 | 0.42823 | | | | |
| ⁴ He _{crushed} (ccSTP) | $7.49 	imes 10^{-11} \pm 5.41 	imes 10^{-12}$ | $4.27 	imes 10^{-10} \pm 7.30 	imes 10^{-12}$ | | | | |
| ³ He/ ⁴ He _{crushed} (R/Ra) | $\textbf{8.88} \pm \textbf{0.37}$ | 8.08 ± 0.58 | | | | |
| ⁴ He _{melt} (cc STP/g) | $2.24 	imes 10^{-10} \pm 1.62 	imes 10^{-11}$ | $9.97 	imes 10^{-10} \pm 1.70 	imes 10^{-11}$ | | | | |
| ³ He/ ⁴ He _{melt} (R/Ra) | 25.8 ± 1.7 | 28.1 \pm 1.2 | | | | |
| 3He _{cosmo} (atoms/g) | $1.41 	imes 10^5 \pm 2.17 	imes 10^4$ | $7.43 	imes 10^5 \pm 5.29 	imes 10^4$ | | | | |
| Age (years) St scaling | 368 ± 140 | 2087 ± 546 | | | | |
| Age (years) LSDn scaling | 513 \pm 194 | $\textbf{2507} \pm \textbf{656}$ | | | | |
| | | | | | | |

Note: The ⁴He procedural blank is $8\pm1\times10^{-12}$ cc standard temperature and pressure (STP). Exposure ages calculated using Lifton-Sato-Dunai (LSDn) scaling method correspond to the flux-based version of Lifton et al. (2014) scaling (bold, preferred ages), whereas St uses the Lal (1991)/Stone (2000) scaling model. Uncertainties are $\pm2\sigma$ external. R/Ra is the 3 He/ 4 He ratio in the sample divided by that of the atmosphere (Ra = 1.4×10^{-6}).

ships, we concur with Moreno and Lara (2007) that cone growth at Choshuenco and the oldest portion of Mocho began simultaneously. Lavas of Mca terminate at 400–600 masl, and lower elevations are difficult to access owing to dense vegetation. Glacially enhanced erosion exposes lava packages 500–700 m thick on the southern flank and 800–1000 m thick on the northern flank of Choshuenco. From these relationships, we conservatively estimate a minimum volume of 50 km³ that accounts for erosion. Projecting lava flow dips on the SW flank to the center of the Mocho edifice supports a volume estimate of \sim 80 km³.

Andesitas basálticas de Punahue (Abp; 130–45 ka)

Note: masl-meters above sea level.

Unit *Abp* includes crystal-rich (20%–30%) olivine- and pyroxene-bearing lavas and tephra of basaltic andesitic to andesitic composition (52.5–66.5 wt% SiO_2 ; Fig. 5) and one dacitic lava (66.6 wt% SiO_2 ; Fig. 5). A 100-m-thick escarpment located on the eastern flank comprises an intercalation of lavas and tephras from which an age of 128.5 ± 12.7 ka was obtained from a basaltic andesitic lava (Table 1). This

age agrees with the $130 \pm 30 \text{ ka}^{40}\text{Ar}/^{39}\text{Ar}$ age reported by Moreno and Lara (2007; Table S5) and represents the older portion of this unit. The most prominent outcrops are on the northern flank of Mocho-Choshuenco, where a 500-m-thick package of several lavas terminates ~2 km north of the village of Punahue. A basaltic andesitic lava here yields an age of 110.3 ± 6.3 ka. On the southern flank, another package of lavas reaches even lower altitudes. The toe of a basaltic andesitic lava flow 15 km southwest of the Mocho cone at 430 masl yields an age of 114.2 ± 14.2 ka (Fig. 2). Based on these relationships, the thickness of this package of lavas is estimated at 300-500 m. Cone growth continued with the eruption of basaltic andesitic lavas intercalated with one dacitic lava $(81.1 \pm 1.9 \text{ ka})$, which terminates $\sim 3.5 \text{ km}$ east of the modern Mocho summit cone (Fig. 3). If lava flows were emplaced between 80 and 45 ka, they are either no longer preserved owing to glacial erosion, or we have failed to sample them. Our interpretation of lava thickness suggests a minimum volume of 40 km3 that we use with caution, given the probable extent of glacial erosion.

Andesitas basálticas del Río Blanco (Arb; 45–18 ka)

On the western flank of the modern Mocho cone are lavas that erupted between 45 and 18 ka. As with units Mca and Abp, these crystalrich (20%–30%), olivine- and pyroxene-bearing basaltic andesitic and minor andesitic flows (52.5-57.8 wt% SiO₂; Fig. 5) share a wide compositional range in MgO (Fig. 4) and incompatible elements (Fig. 6) with similar wt% SiO₂. A platy-jointed lava (55.9 wt% SiO₂) at 1617 masl yields a plateau age of 45.4 ± 3.7 ka. A lava flow (57.8 wt% SiO₂) on the eastern flank overlying dacite of the Abp unit yields a similar age of 44.9 ± 7.5 ka and, on the southern flank, a strongly glaciated basaltic andesitic (53.5 wt% SiO_2) outcrop is dated at 37.1 \pm 7.6 ka (Fig. 8). Subangular to rounded cobbles of granitoid lithologies are glacial erratics that were deposited onto these lava outcrops by melting ice (Figs. 2 and 3). On the northeastern flank, the unit is directly overlain by basaltic andesitic lava flows that erupted between 26 and 18 ka. Similar stratigraphic relationships are observed on the southwestern flank in lava flows dated at 18.0 ± 3.1 and 18.9 ± 3.1 ka that overlie unit Mca. The indistinguishable ages (18.0 \pm 3.1, 18.6 \pm 2.6, and 18.9 \pm 3.1 ka; weighted mean = 18.5 ± 1.7 ka; Table 1; Fig. 4) and compositions (53.9-54.0 wt% SiO₂) of lavas on the western flank suggest that they are from the same flow or erupted synchronously. We estimate this unit to be 50 m thick with a minimum volume of 0.7 km³. Based on stratigraphic relationships, we suggest that the incompatible element-poor basaltic andesites erupted between 45 and 37 ka, followed by incompatible element-rich basaltic andesites from 26 to 18 ka. We found no lavas with ages of between 37 and 26 ka. This finding may reflect either a minimal eruptive volume or sampling bias, as discussed below.

Dacitas y Andesitas del Río Truful (Drt; 18–12 ka)

During the peak of the local LGM and subsequent rapid deglaciation, siliceous andesite to

TABLE 3. CHARACTERISTICS OF LAVA-DOMINATED UNITS

| INDEE 6. OF INTEROCULAR DOMINANTED ON TO | | | | | | | |
|---|--|-------------------|--------------------------|-----------------|--|--|--|
| Unit (abbreviation) | Magma compositions | Age (ka) | Altitude terminus (masl) | Volume (km³) | Characteristics (Fig. 8) | | |
| Andesitas y Dacitas del Mocho (Adm) | Andesite, dacite, and basaltic andesites (minor) | 1.6-recent | 900–1400 | 0.3 | Vertical columns (meters) | | |
| Andesitas y Dacitas del Estero Chumpulli (Adec) | Andesite, dacite, and basaltic andesites (minor) | 12–1.6 | 200–1500 | 0.3 | Vertical columns (meters) | | |
| Dacitas del Estero Pirinel (Dep) | Dacite | 11.5-8 | 350-450 | 5 | | | |
| Dacitas y Andesitas del Río Truful (<i>Drt</i>) | Dacite and andesite (minor) | 18–12 | 680–1800 | 6.2 | Variable column orientations, platy jointing (decimeters), radial jointing, finger-like ridges, inverted topography, autobreciate carapace | | |
| Andesitas basálticas del Río Blanco (Arb) | Basaltic andesite | 45–18 | 1400–1700 | 0.7 | Variable column orientations, platy jointing (decimeters), cliffs (\sim 30 m) | | |
| Andesitas basálticas de Punahue (Abp) Mocho-Choshuenco Ancestral (Mca) | Basaltic andesite and andesite Basaltic andesite, andesite, and dacite (minor) | 130–45 300–130 | 200–1000 400–600 | 40 80 | Vertical columns (meters) Vertical columns (meters) | | |

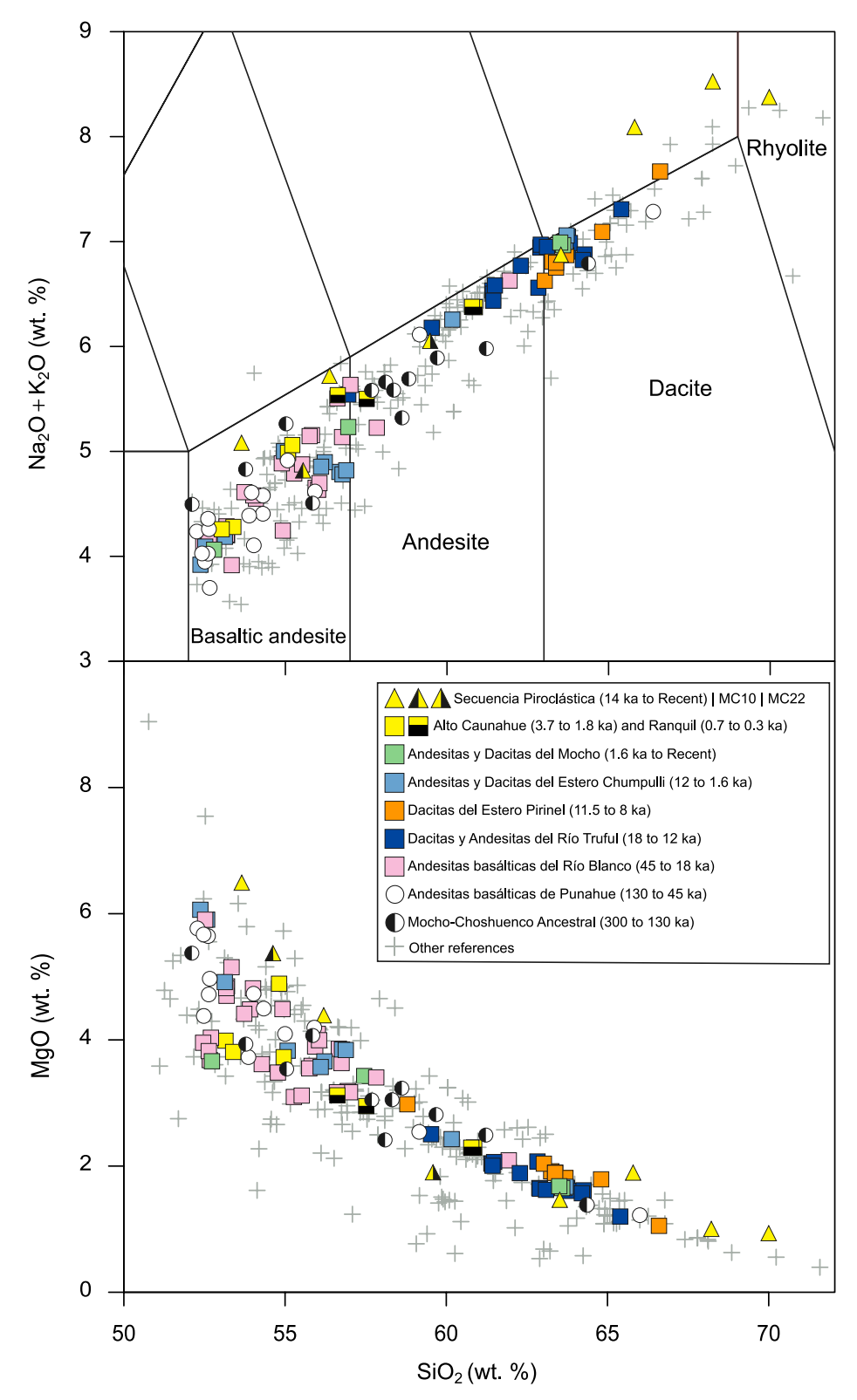


Figure 5. Major element compositions of whole-rock lavas (square) and tephra glass shards (triangles). Secuencia Piroclástica data are average glass shard composition determined by electron probe microanalysis. Crosses are whole rock data from McMillan et al. (1989), Echegaray (2004), Gardeweg (2010), and Rawson et al. (2015, 2016b).

crystal-poor dacite (59.5–64.3 wt% SiO₂; Fig. 5) erupted, whereas basaltic andesites did not. On the western, eastern, and southeastern flanks, this package of lavas overlies the Abp unit, which comprises lavas as young at 18 ka. Outcrops of Drt lavas show conspicuous and abundant lava-ice interaction textures (see below; Fig. 8), including morphological evidence of ice-confinement (Figs. 8A and 8B) and highly variable orientations and sizes of polygonal jointing (Figs. 8D and 8F). They give ⁴⁰Ar/³⁹Ar ages of between 19.7 \pm 3.2 and 16.2 \pm 2.6 ka (Table 1). A compositionally similar dacitic lava (64.2 wt% SiO₂) near the top of this package, which is truncated at the caldera rim, gives a comparable age of 16.6 ± 2.4 ka. Thus, the latter finding gives a maximum age for collapse of the caldera that is likely associated with eruption of the MC2 or Neltume rhyolites (Fig. 3).

On the western flank, a dacitic lava (63.8 wt% SiO_2) flow, dated at 19.7 ± 3.2 ka, is indistinguishable in age from the underlying 18.7 ± 2.0 ka basaltic andesites of the Arb unit. Moreover, Drt lavas are mantled by the 11.5 ka Neltume tephra, which is consistent with our chronostratigraphy (Figs. 7B and 8C). Because lava flows of this unit are overlain by a basaltic andesitic lava dated at 12 ka, we infer that Drt eruptions had ceased by this time.

Lavas from these units follow both the incompatible element-rich and element-poor trends. Based on stratigraphic relationships, we argue that the incompatible element-rich magma erupted between 17 and 16 ka, followed by the incompatible element-poor dacitic magma between 16 and 12 ka. The thickness of *Drt* lavas ranges from 30 to 100 m, with an estimated volume of 1.0 km³.

Dacitas del Estero Pirinel (Dep; 11.5–8 ka)

Crystal-poor dacitic lavas (63.0–66.6 wt% SiO_2 ; Fig. 5) that immediately overlie the main Choshuenco edifice at \sim 1750 masl are assigned to unit Dep. These lava flows terminate only 3 km from the town of Choshuenco, 4 km from Enco, and are incised by the Estero Pirinel (Pirinel Creek, Fig. 2). Age determinations of $11.3 \pm 3.7, 9.4 \pm 2.9$, and 8.0 ± 2.5 ka are from outcrops at elevations of between 300 and 450 masl (Figs. 3 and 4) and are consistent with the observation that lavas from the Dep unit overlie the 11.5 ka Neltume tephra. The thickness estimated for this unit is \sim 50 m, which gives a volume of \sim 1.3 km³.

Andesitas y Dacitas del Estero Chumpulli (Adec; 12–1.6 ka)

A basaltic andesitic lava (52.5 wt% SiO_2) dated at 12.4 \pm 4.7 ka (Fig. 4) represents the

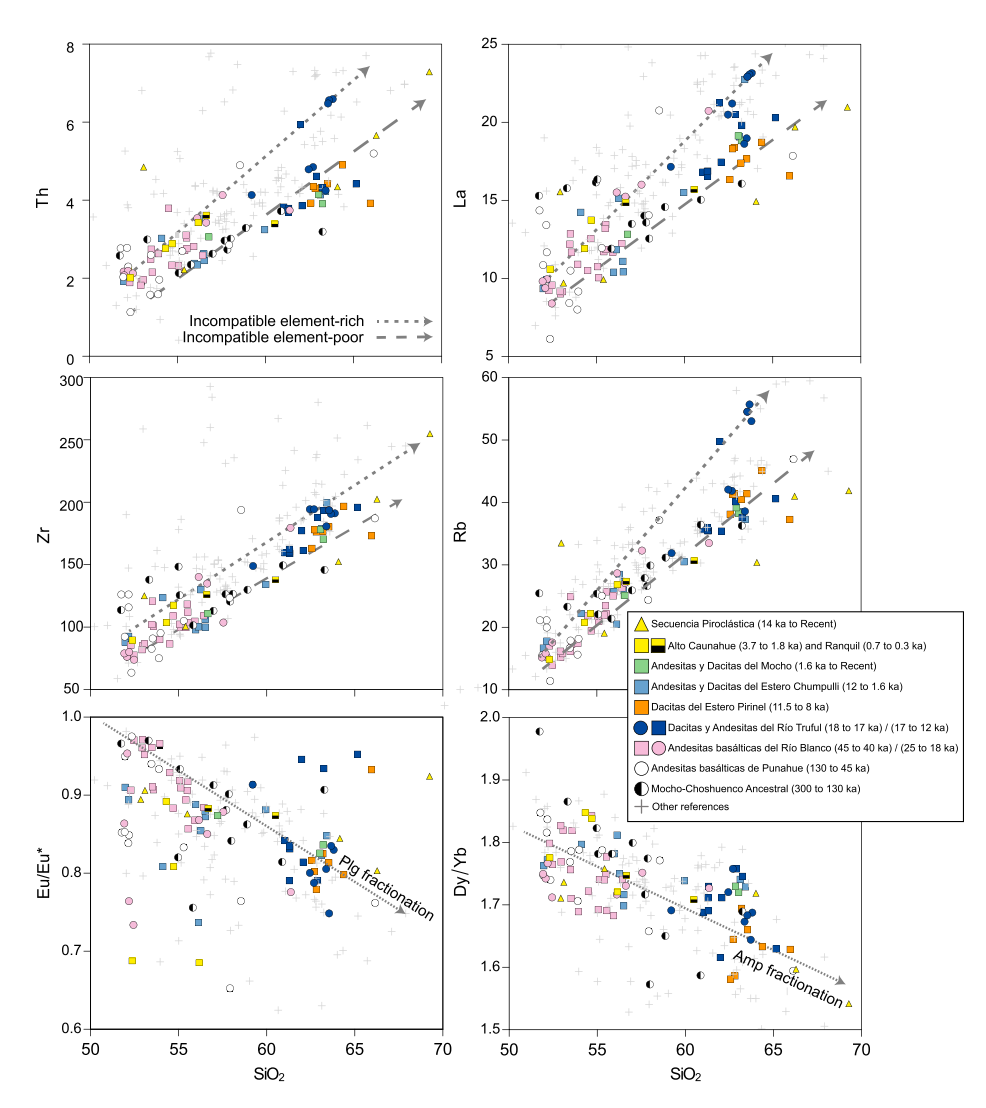


Figure 6. Select trace element concentrations (ppm) and ratios versus SiO_2 (wt%) of whole-rock Mocho-Choshuenco lavas and tephras. The Secuencia Piroclástica (triangles) data are average glass shard compositions. Eu/Eu* was calculated following Rollinson and Pease (2021) using normal mid-oceanic-ridge basalt compositions from Sun and McDonough (1989). Crosses show data from McMillan et al. (1989) and Rawson et al. (2016b).

onset of effusive eruptions that formed the Adec unit. This flow overlies dacites from unit Drt at 1470 masl. Near the caldera rim, a glassy dacitic lava (63.6 wt% SiO₂) yields an age of 6.5 ± 2.5 ka and represents a post-caldera eruption. An andesitic lava (56.1 wt% SiO₂) at much lower elevation (1580 masl) that overlies the 11.5 ka Neltume tephra yields an age of 4.4 ± 3.4 ka (Fig. 7). Because this lava is also overlain by the 1.6 ka Enco ignimbrite, we suggest this is the minimum age of this unit. Other lavas directly overlying unit Arb and covered by the 1.6 ka Enco ignimbrite did not yield detectable ⁴⁰Ar*, which strongly suggests that they erupted between 5 and 1.6 ka. Hence, we incorporate them into this 0.3 km³ unit. Based on our age and stratigraphic constraints for this unit, it is

likely that both the Mocho and Choshuenco cones were erupting synchronously between 12 and 8 ka.

Andesitas y Dacitas del Mocho (Adm; 1.6 ka to Recent)

The youngest lavas on Mocho-Choshuenco are andesites to crystal-poor dacites (56.7–64.0 wt% SiO₂; Fig. 5) that erupted from the modern Mocho cone and are not covered by the 1.6 ka Enco ignimbrite. The most prominent lavas are on the western flank and partially overlap the *Adec* unit. The vent from the 1 November 1864 eruption (Vidal Gormaz, 1869; Petit-Breuilh, 2004; Echegaray, 2004) is on the southernmost side of this unit (Figs. 2 and 7). The 4-km-long, 30-m-thick dacitic lava (Fig. 7) was

accompanied by pyroclastic flows that reached Lago Panguipulli (Fig. 2) and killed many of the Indigenous people living in the vicinity (Vidal Gormaz, 1869). The volume is estimated at 0.5 km³. Rawson et al. (2015) suggest that the basaltic andesitic Riñihue tephra is the explosive component of the 1864 eruption. Based on the silicic composition of lava flow (64 wt% SiO₂), we suggest that the Riñihue tephra corresponds to an older, likely historic eruption. Petit-Breuilh (2004) describes two eruptions from Mocho-Choshuenco in 1759 and 1777, and Göll (1904) describes one in 1822. Descriptions of two later eruptions in 1937 (Petit-Breuilh, 2004; Fontjin et al., 2014; Edwards et al., 2020; Global Volcanism Program, 2023) and 1955 (Petit-Breuilh, 2004) are controversial. After thoroughly searching local newspapers from 1936, 1937, 1954, and 1955, we propose that the 1937 and 1955 eruptions are mistakenly attributed to Mocho-Choshuenco and correspond instead to eruptions from Sollipulli and Carrán-Los Venados volcanoes, respectively ("Una Erupción del Volcán Mocho," 1937; "Choshuenco," 1955). Hence, we concur with Moreno and Lara (2007) that the last eruption of Mocho-Choshuenco occurred in 1864 (from a new cone named Chaiquemahuida; González-Ferrán, 1995).

Secuencia Piroclástica (Hp; 14 ka to Recent)

Twenty-seven tephras were identified by Rawson et al. (2015) and comprise the Secuencia Piroclástica unit (Moreno and Lara, 2007). Due to the number of potential vents, no confident correlation with the Alto Caunahue (south) or Ranquil (east) cones is possible (Rawson et al., 2015). Here, we refine these units using tephrostratigraphic correlations based on two ³He age determinations and glass shard compositions.

Alto Caunahue (Hac; 3.7-1.8 ka). Thirteen Holocene pyroclastic cones of basaltic andesitic composition (53.4-56.6 wt% SiO₂; Fig. 5) are located on the southern flank of Mocho-Choshuenco, and sit unconformably atop the Mca and Abp units. The craters are 100- to 250-m-high and have diameters that range from 200 to 400 m. The lava flows (<10 m thick) are clearly overlain by the 1.6 ka Enco ignimbrite (Moreno and Lara, 2007). A 3He surface exposure age of a bomb from Hac displaying breadcrust texture (55.0 wt% SiO₂) indicates an eruption at 2.5 ± 0.7 ka (Figs. 2 and 7C). Based on the minimum age determination, prevailing wind direction, and compositional similarity, we correlate the Hac unit with MC10H tephra (Fig. 5; Rawson et al., 2015). Given Rawson et al.'s (2015) maximum modeled age of 3.7 ka for MC10H (within the Grupo Fui unit), coupled with the 3He age and its uncertainty,



Figure 7. Key field relations on Mocho-Choshuenco. (A) View from helicopter to the southwest of the northern flank showing deeply eroded Pleistocene Choshuenco edifice (unit Mocho-Choshuenco Ancestral, Mca) including a dike complex buried by a prominent lateral moraine. (B) View west of Ranquil cone (unit Hr) overlying lavas of unit Dacitas y Andesitas del Río Truful (Drt). Lava-forming cliffs of the unit Andesitas basálticas del Río Blanco (Arb), from which Drt dacites flowed. is also shown. Yellow Neltume tephra is observed on the highest slopes overlying lavas of the unit Andesitas basálticas de Punahue (Abp). Unit Andesitas y Dacitas del Mocho (Adm) is also observed on the current Mocho cone. (C) View southwest of unit Alto Caunahue (Hac) overlying lavas of Mca, and a large 3He bomb dated at 2.5 ka. (D) View west of truncated lava at the caldera rim (Drt). Holocene lavas from the current Mocho cone are also shown (Adm). (E) View west of Chaiquemahuida flow from A.D. 1864 banked against Lago Ranco Formation and overlying lavas from units Adm and Dacitas del Estero Chumpulli (Adec). (F) View toward the east of 4.4 ka lava of unit Adec overlying lavas from unit Mca and a lateral moraine. Yellow Neltume tephra mantles the slope of the Choshuenco edifice.

we suggest that these lavas and tephras were emplaced between ca. 3.7 and 1.8 ka. Following field observations and dimensions reported in Moreno and Lara (2007), we estimate a volume of 0.5 km³ for the cones and 0.1 km³ for the lavas, which totals 0.6 km³ for the entire unit.

Ranquil (Hr; 0.7–0.3 ka). The Ranquil unit comprises four Holocene pyroclastic basaltic andesitic to andesitic cones (54.9–60.9 wt% SiO₂; Fig. 5) located in the northeastern flank of Mocho-Choshuenco between 1100 masl and 1600 masl. The cones have diameters of 250–600 m and are 100–200 m high. A 3 He surface exposure age on a bomb with bread-crust texture (54.9 wt% SiO₂) on the rim of the highest cone (1600 masl) indicates an eruption at 0.5 ± 0.2

ka (Figs. 2 and 7). This cone is not covered by the 1.6 ka Enco ignimbrite, which indicates that it indeed erupted during the past 1.6 k.y. Moreover, this minimum age determination, along with the composition of the bomb, suggests a stratigraphic correlation with the MC22 tephra (0.5-0.3 ka) of Rawson et al. (2015; Fig. 5). Taking uncertainties into account, we suggest that unit Hr ranges from 0.7 to 0.3 ka. The volume of the four cones is $\sim 0.6 \text{ km}^3$.

Lava-Ice Interactions

Features resulting from lava flow and ice interaction include subtle changes in the size and shape of individual flow lobes (Edwards et al.,

2015) and massive cliffs that are interpreted as the impounding of lavas by walls of ice (Edwards and Russell, 2002; Lescinsky and Fink, 1998; Conway et al., 2015; Mixon et al., 2021). Pervasive, smaller diameter joints (<0.5 m) with non-vertical orientations (Figs. 8D and 8F) are also consistent with lava cooling owing to contact with meltwater or ice. An eruption of intermediate composition in 2010 from Eyjafjallajökull volcano, Iceland (Oddsson et al., 2016), shows that lavas can exploit water drainage channels in ice at the base of a glacier to advance subglacially. Jointing can be ambiguous as an indication of ice contact (Smellie and Edwards, 2016). Given that Mocho-Choshuenco presently has a small glacier filling the caldera at its summit, it

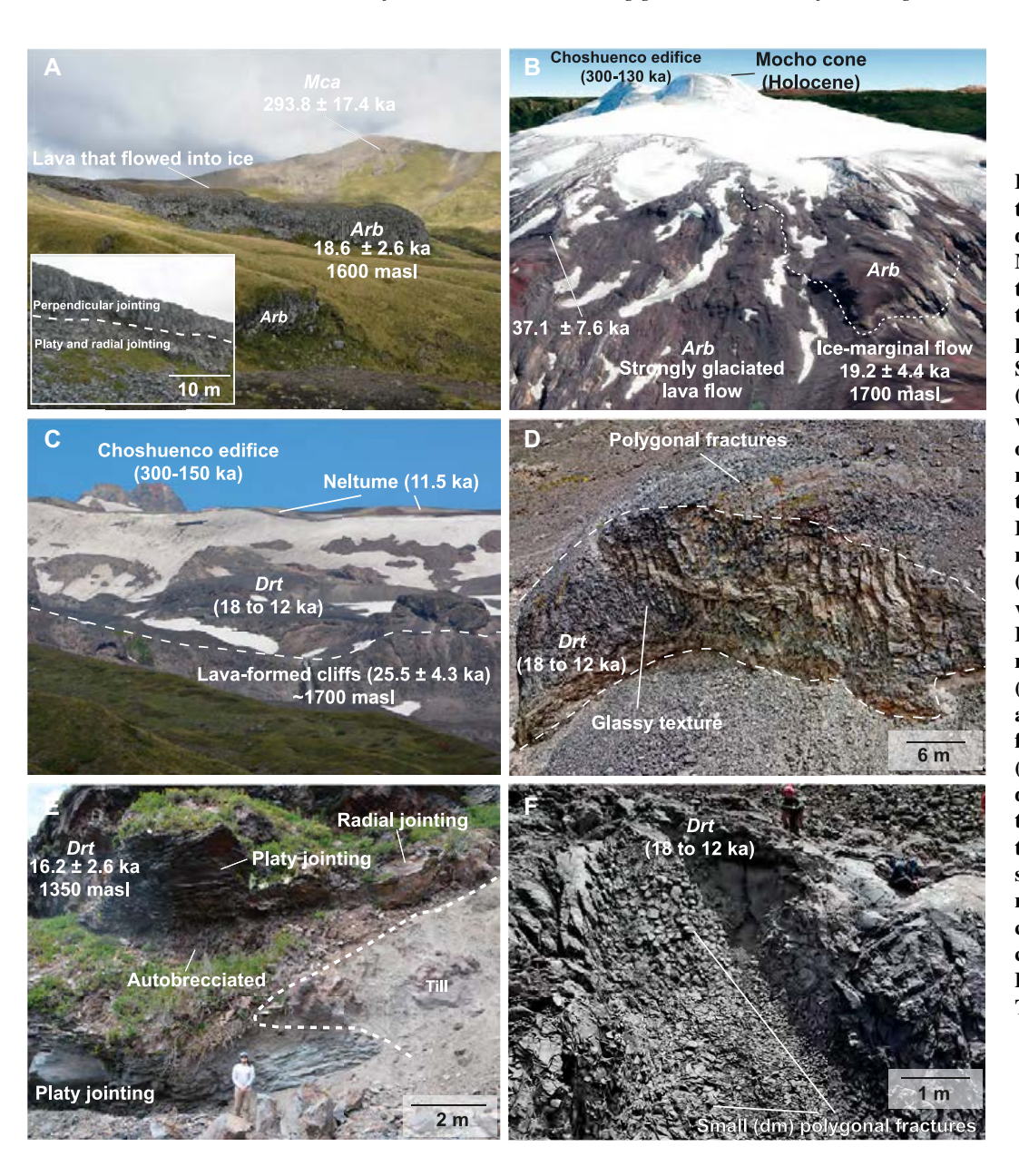


Figure 8. Lava-ice contact relationships and textures in lavas dated between 26 and 16 ka at Mocho-Choshuenco. (A) View to the south of a 18.6 ka lava that is inferred to have been impounded by the Patagonian Ice Sheet at 1600 m above sea level (masl); the oldest preserved lavas of Mocho-Choshuenco are on the horizon. (B) View to the north of 19.2 ka lava inferred to have been impounded by the Patagonian Ice Sheet at 1700 masl on the southern flank (Google Earth image). (C) East view of lava-formed cliffs by Patagonian Ice Sheet at \sim 1700 masl along the western flank. (D) View to the east from an aerial drone of lava-ice contact features in lava-formed cliffs. (E) View to the south of lava dated at 16 ka on top of and intercalated with till. (F) View to the east from an aerial drone of small (decimeter-scale) polygonal fractures in lava-formed cliffs. Arb-Andesitas basálticas del Río Blanco unit: Drt-Dacitas y Andesitas del Río Truful unit.

seems likely that the summit vents have been proximal to ice for much of their eruptive history.

Lava-ice interactions are expressed in the *Arb* and *Drt* units, including overthickening of flows that now form cliffs of up to 30 m high (Figs. 8 and 9), small-diameter and radial columnar joints, and ridge-like lava morphologies. Distinct platy jointing is also pervasive in several lavas that are interpreted to have been emplaced subglacially. While the connections between this style of jointing and emplacement environments are as yet ambiguous (Lescinsky and Fink, 1998), they are frequently found in glaciovolcanic environments (Smellie and Edwards, 2016). Also, whereas many of these features likely indicate the presence of ice during eruptions, it is more difficult to confidently determine whether

the ice was part of a local expansion of the Mocho-Choshuenco ice cap into alpine glaciers, or if it was the margin of massive, valley-filling lobes of the Patagonian Ice Sheet. Whereas jointing above 1800 masl is the most ambiguous, the presence of jointed lava-formed cliffs at lower elevations likely requires ice that is too thick to have formed from the local Mocho-Choshuenco ice cap. Moreover, the presence of basaltic andesites of the same age (26–18 ka, Arb unit) that thicken downhill and form cliffs at similar elevations (1550-1700 masl) around the flanks of the volcano favor a role for >1500-m-thick lobes of the Patagonian Ice Sheet that surrounded the edifice between 35 and 18 ka. Particularly on the eastern flank-close to Río Truful—lavas emplaced at 26 ka (Arb unit) were

confined by the Patagonian Ice Sheet at 1550 masl. Subsequently, at 18 ka, *Drt* dacites flowed over these basaltic andesites. At that time, the Patagonian Ice Sheet likely had begun to shrink and retreat (Denton et al., 1999, 2021; Glasser et al., 2008; Moreno et al., 2015; Davies et al., 2020). The pervasive small-diameter radial and platy jointing, along with brecciated surfaces on the dacites (Fig. 8D), suggest a supraglacial flow, and hence that the elevation of the local cap was between the layers of basaltic andesites and dacites (Fig. 9). The dacite becomes channelized as it melts through the underlying ice and terminates in melting ice or supraglacial lake to form a lava-fed delta (Fig. 9).

Lavas and erratic blocks on the flanks of the edifice provide valuable information about

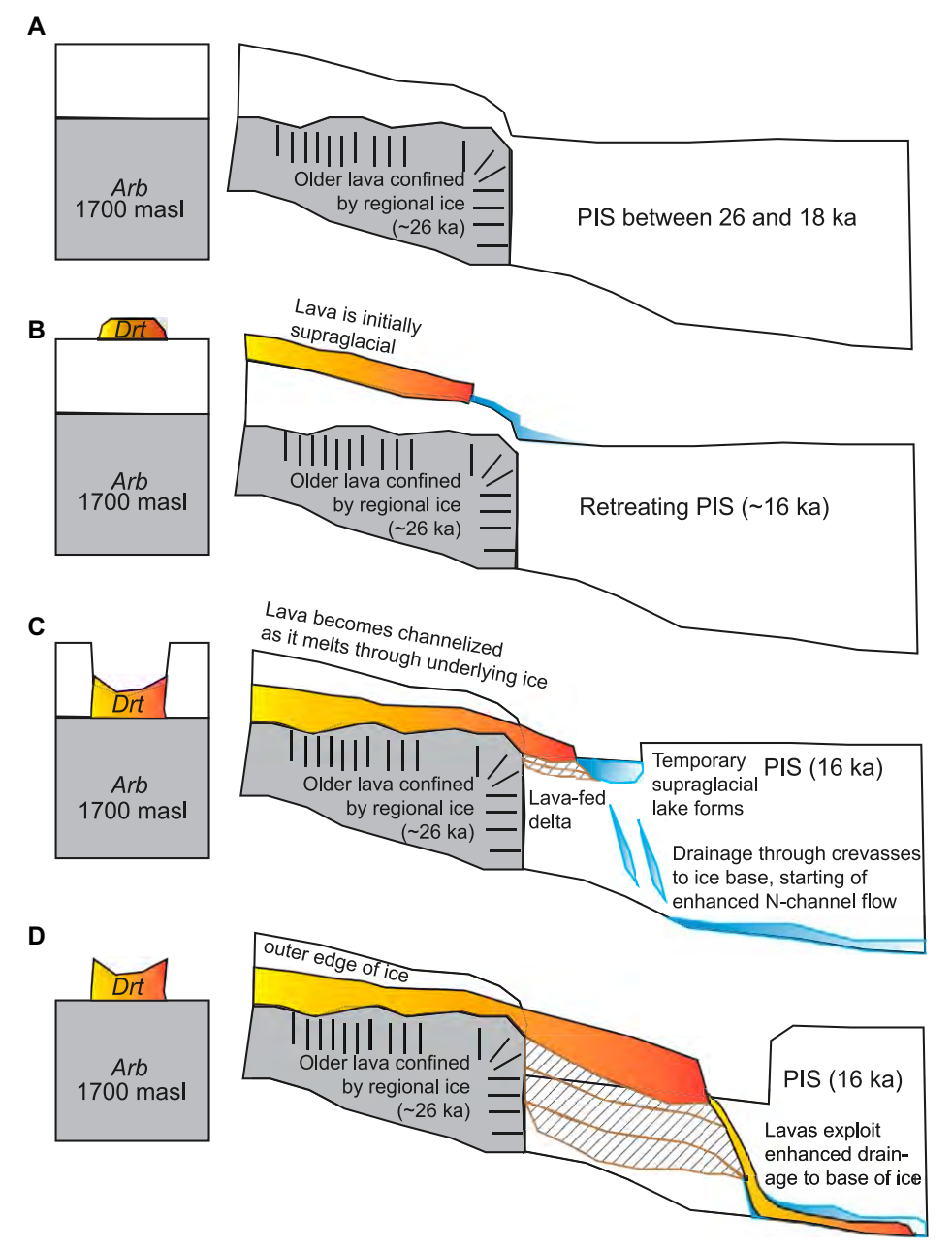


Figure 9. Lava-fed delta model. (A) Basaltic andesites from the Andesitas basálticas del Río Blanco (*Arb*) unit were impounded by the Patagonian Ice Sheet (PIS) at ca. 26 ka, forming cliffs that were then occupied by the Patagonian Ice Sheet at 1500–1700 m above sea level (masl) between 26 and 20 ka (Figs. 8D and 8F). Ice on top of the edilice should have been comparatively thinner than in the surrounding valleys (Cuzzone et al., 2024). (B) As the Patagonian Ice Sheet retreated between 18 and 16 ka, dacite from unit *Drt* flowed onto it. (C) Lava is channelized as it melts the ice to form a lava-fed delta. (D) Dacite flows through the ice and to its base. Lava-ice textures from these outcrops are evident in Figure 8E.

the thickness of the Patagonian Ice Sheet. We discovered numerous subrounded to rounded cobbles of a variety of granitoid lithologies in glacial till that is otherwise comprised of volcanic materials on the eastern flank of the edifice at 1800 masl (Figs. 2 and 3). Although it

is possible that these erratics could have been remobilized in that area, the fact that they are found only at particular elevations and overlying syn-LGM units indicates that the upper surface of the Patagonian Ice Sheet reached this altitude (or higher) during the LGM. Coupled with the areas where the Arb unit forms cliffs and the Drt unit has pervasive radial and platy jointing, we infer that the upper surface of the Patagonian Ice Sheet was at 1550-1650 masl on the western and northern flanks, 1800 masl on the eastern flank, and 1700-1800 masl along the southern flanks. Current valley floors surrounding the volcano are at 200-500 masl, and thus the Patagonian Ice Sheet locally varied from \sim 1300 to 1700 m in thickness during the LGM. Our interpretation is consistent with the \sim 300-m-deep, U-shaped glacial valleys on the southern and eastern flanks of the edifice (Fig. 2). These estimates are also consistent with the geologic and geochronologic constraints on the areal extent and temporal evolution of the Patagonian Ice Sheet (Moreno et al., 2015; Davies et al., 2020; Alloway et al., 2022), as well as with climate-driven numerical models of Patagonian Ice Sheet thickness during the past 25 k.y. (Cuzzone et al., 2024). The lack of lavaice contact features in outcrops from the Dep unit and their termination at lower elevations, 300-400 masl, indicates that the Patagonian Ice Sheet had retreated substantially by 12 ka, leaving behind only small mountain glaciers (Denton et al., 1999; Moreno et al., 2015; Alloway et al., 2022; Cuzzone et al., 2024).

Compositional Evolution

The long-term evolution of magmas beneath Mocho-Choshuenco is recorded by incompatible element-poor eruptions from both Mocho and Choshuenco edifices. However, the late Pleistocene to mid-Holocene is characterized by incompatible element-rich basaltic andesites (26–18 ka) and dacites (18–17 ka), and silicic eruptions as young as 8 ka. In addition to these compositional shifts, variation in oxygen fugacity estimated from successive eruptive products by Rawson et al. (2015; Fig. S3) suggests that the magma was sourced from discrete reservoirs separated in space and time.

Long-Term Evolution of the Magma Plumbing System

Mocho-Choshuenco volcanism began at ca. 300 ka, with mainly basaltic andesites to andesites that erupted until 37 ka (52.1–61.2 wt% SiO₂; Fig. 10A, *Mca*, *Abp*, and *Arb* units), followed by a reduced level of volcanism until 26 ka, when basaltic andesitic (52.5–59.2 wt% SiO₂) eruptions resumed (Fig. 10A). At 18 ka, eruptions shifted to dacitic composition (61.4–64.3 wt% SiO₂; Fig. 10A, *Drt* unit), followed by the explosive eruptions of Neltume rhyolite at 11.5 ka, Pirehueico rhyodacite at 10.2 ka, MC6 dacite (9.0 ka), and Huilo dacite at 8.2 ka (Fig. 10A, *Dep* unit). We argue that these latter three eruptions may have come from Choshuenco, with

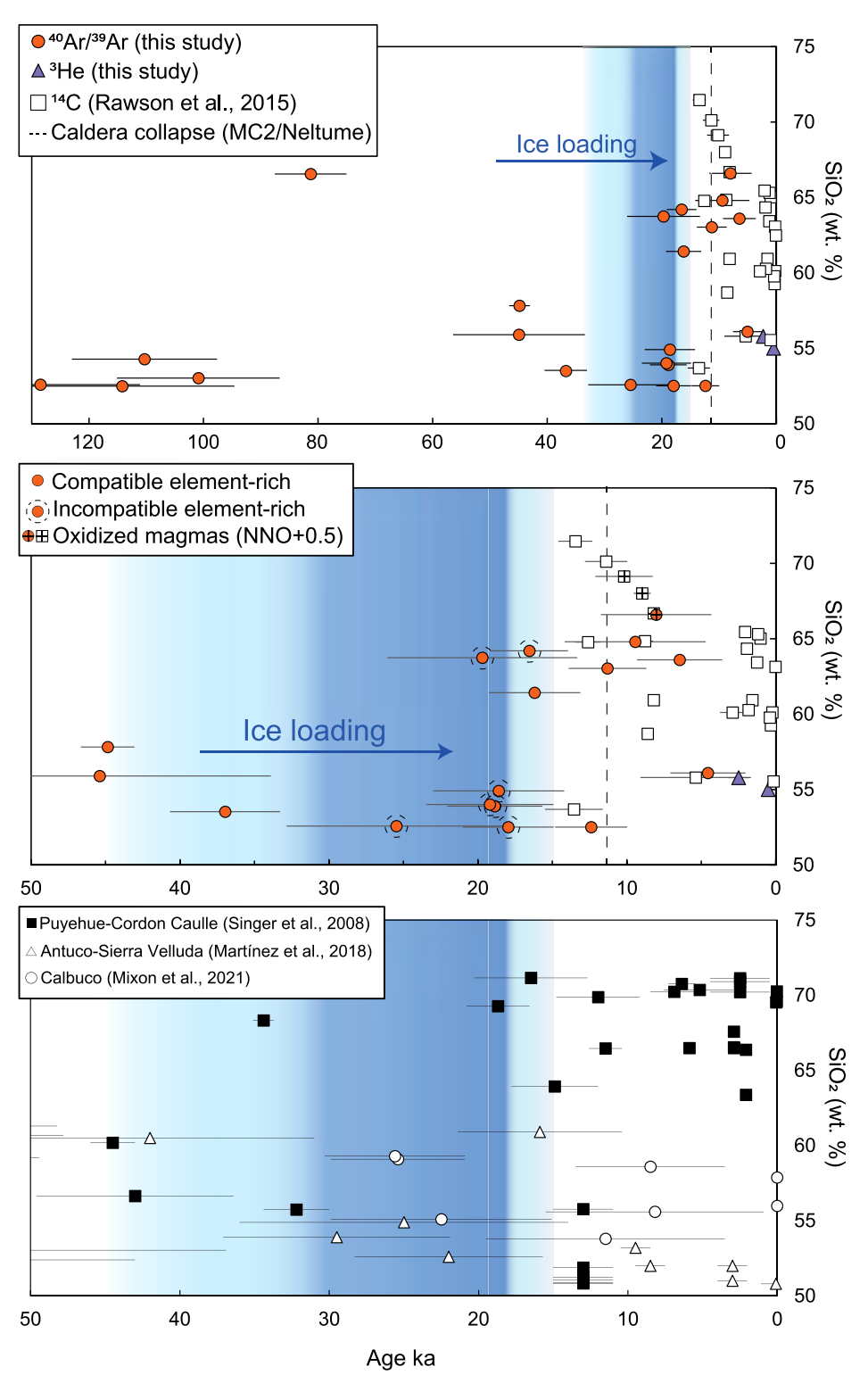


Figure 10. Magmatic evolution of Mocho-Choshuenco from 130 ka to present. ¹⁴C ages are averages for tephra deposits from Rawson et al. (2015). Grupo Fui tephra (MC10) comprise all subunits. Growth of ice is indicated at ca. 45 ka but is more extended during the local Last Glacial Maximum and reaches a maximum at 18 ka. Dashed line represents edifice collapse at 11.5 ka associated with the Neltume rhyolite eruption. Middle and bottom panel illustrate evolution of Mocho-Choshuenco and other well-dated Andean Southern Volcanic Zone volcanoes during the past 50 k.y. (Singer et al., 2008; Martínez et al., 2018; Mixon et al., 2021).

lavas from the Dep unit being their effusive expression. The oxidation states of magmas that erupted to generate these two groups of tephras (NNO + 0.5 in Pirehueico, MC6 and Huilo versus NNO in Neltume, Fig. S3; Rawson et al., 2015) suggest that the reservoir below the Choshuenco cone, although compositionally similar, was more oxidized relative to that sourcing eruptions from the composite cone. Another profound shift is observed following those eruptions when a wide spectrum of magmas ranging from basaltic andesites to dacites (52.5–64 wt% SiO_2) erupted during the Holocene from the main cone (Adec and Adm units) and minor eruptive centers (Hac and Hr units).

Evolution of Incompatible Element-Rich and Element-Poor Magma between 45 and 16 ka

Both basaltic andesites (Arb unit) and dacites (Drt unit) at Mocho-Choshuenco show a wide range of incompatible element contents at a constant SiO₂ content, which indicates at least two distinct differentiation pathways (Fig. 6). Fractional crystallization of at least two, and possibly more, parental magmas is the main process by which intermediate and silicic compositions originate. The spread in light rare earth element contents (e.g., La) at a constant SiO₂ (Fig. 6) supports an interpretation that basaltic andesitic magmas reflect a range of degrees of partial melting of mantle source rocks (e.g., Hickey-Vargas et al., 2016; Rawson et al., 2016b; Morgado et al., 2019). Trace element ratios such as Eu/Eu* and Dy/Yb indicate that plagioclase and amphibole are prominent among fractionated minerals (Fig. 6; Davidson et al., 2007). The large range of MgO at a constant value of 52 wt% SiO₂ suggests that olivine accumulation was also important (Fig. 5; Sisson and Grove, 1993). The wide range of Rb concentration in the basaltic andesites is also consistent with the hypothesis that multiple parental magmas may have fractionated to produce silicic magmas (Fig. 6) and that mingling and mixing of basaltic andesitic and dacitic magma also may have played a lesser role in producing andesites. Incompatible element variability in lavas from 37 to 16 ka could reflect the assimilation of Paleozoic metamorphic and/or granitoid rocks, as suggested by McMillan et al. (1989). In contrast, lavas that erupted before and after the local LGM contain 20-55 ppm Rb, respectively, which likely reflects fractional crystallization of basaltic andesitic parental magmas. Following the eruption of incompatible element-poor basaltic andesites between 45 and 37 ka, magma may have stalled and assimilated Paleozoic wall rocks in a deeper portion of the crust, causing Th, Zr, and Rb concentrations to increase prior to eruptions between 26 and 18 ka.

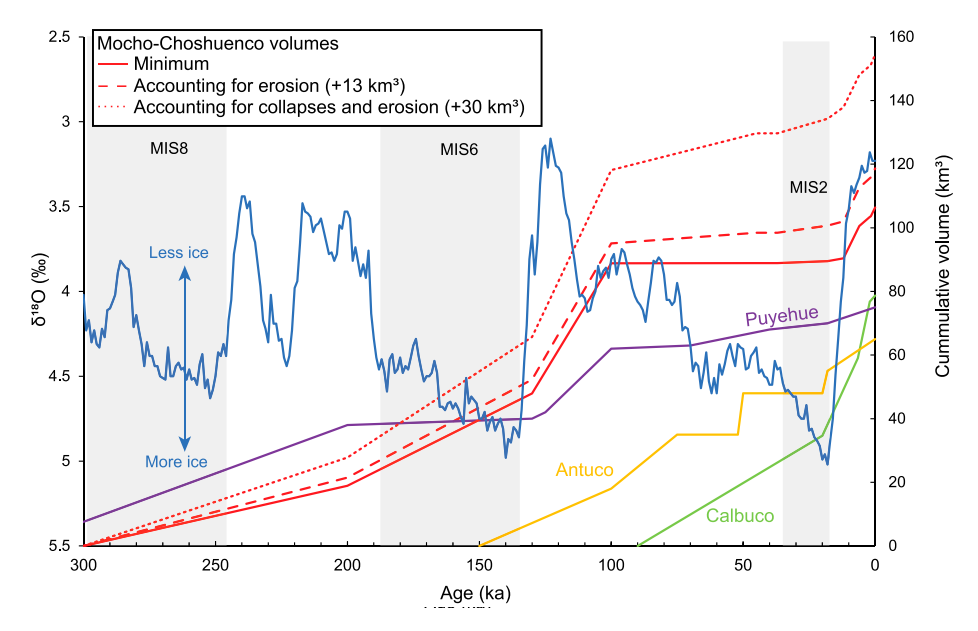


Figure 11. Cumulative volume for Mocho-Choshuenco estimated as discussed in the main text. Eroded volume is estimated at 13 km³. Minimum Puyehue, Antuco, and Calbuco curves are from Singer et al. (2008), Martínez et al. (2018), and Mixon et al. (2021), respectively. Global marine δ¹⁸O curve in blue and marine isotope stages (MISs) are from Lisiecki and Raymo (2005).

Compartmentalized Mid- to Upper-Crustal Reservoirs and Their Evolution over Time

The parallel fractionation trends illustrated in Figure 6 that show twofold variations in the concentrations of incompatible trace elements Th, La, Zr, and Rb at a single SiO₂ content, coupled with the order-of-magnitude contrasts in the buffering of oxygen fugacity among successive post-LGM silicic magmas (Fig. S3), are difficult to explain via fractional crystallization, magma mixing, or crustal assimilation operating to modify a single reservoir of magma. Instead, we interpret this evidence as favoring the establishment of spatially and compositionally discrete reservoirs that developed within the larger magma plumbing system. Episodic tapping of the various reservoirs to produce eruptions of compositionally distinctive magma also point to a spatiotemporally complex transcrustal magma plumbing system beneath Mocho-Choshuenco. For example, the eruptions between 45 and 37 ka of incompatible elementpoor basaltic andesite, followed by eruptions between 26 and 17 ka of incompatible elementrich basaltic andesites and dacites separated by only 10 k.y. is unlikely to reflect the internal evolution of a single magma reservoir. After the latter incompatible element-rich reservoir emptied, incompatible element-poor silicic magmas erupted between 16 and 11.5 ka, culminating with the explosive Neltume rhyolite that likely emptied this reservoir and allowed deeper mafic magma to transit through its remains to erupt immediately following collapse of the caldera. At the same

time, a third reservoir, slightly more oxidized (Fig. S3) and hence with higher water than the previously erupted magmas, was likely building up beneath what is now the Choshuenco cone and erupted between 11.5 and 8 ka.

Hence, despite the petrographic similarities among lavas and tephras from Mocho-Choshuenco, contrasting major and trace element differentiation pathways, oxidation states, and compositions of products that erupted less than 2 k.y. apart imply a set of spatially compartmentalized mid- to upper-crustal magma reservoirs that evolved independently from one another.

Time-Volume Relationships

We estimate a total volume of $\sim 106 \text{ km}^3$ for the entire edifice (Fig. 11). The minimum average growth rate of Mocho-Choshuenco is ~ 0.37 km³/k.y. from 300 ka to recent and is comparable to those of many other arc front composite volcanoes (Singer et al., 2008; Mixon et al., 2021). Cone growth increased from 0.18 km³/k.y. between 300 and 200 ka to 0.40 km³/k.y. between 200 and 130 ka. Following the end of the penultimate glaciation at ca. 130 ka, the growth rate increased to 1.36 km3/k.y., which reflects the eruption of extensive basaltic andesitic lava flows that now comprise the older portion of the Abp unit and \sim 80% of the entire composite cone. The remaining 20% of the edifice grew via spurts of relatively rapid

growth, modulated by periods of high erosion. From 100 to 45 ka, 45 to 37 ka, and 37 to 18 ka, the growth rate was <0.02 km³/k.y. (part of the Abp and Arb units) but was followed by orderof-magnitude increases to 0.2 km³/k.y. between 18 and 12 ka, and to 1.7 km³/k.y. from 12 to 8 ka (Drt and Dep units, and the eruptions of MC2, Neltume, Pirehueico, and Huilo). The mid-Holocene is marked by moderate growth at 0.38 km³/k.y. from 6 to 1.6 ka (Fig. 11, the Grupo Fui, Adec, and Hac units) that ticked up to ~ 1 km³/k.y. during the past 1.6 k.y. (units Adm, Hr, Enco, and Hua-Hum). Importantly, these volume estimates do not account for erosion and removal of material that at other nearby Andean Southern Volcanic Zone volcanoes has been estimated to comprise as much as 10%-25% of the current volume of the edifice (details in Figs. S1 and S2). Using the methods outlined above (and in Figs. S1 and S2), we estimate that over the 300 k.y. history of Mocho-Choshuenco cone growth, a minimum of $\sim 13 \text{ km}^3$ —approximately 12% of the current volume-has been eroded and removed. In addition to the prominent Mocho caldera, earlier collapses or edifice failures, for which geological evidence is not preserved or has been buried by subsequent lava flows, could have occurred. Truncated lavas from the Mca unit (Fig. 8A) suggest at least one edifice failure between 300 and 100 ka. Extrapolating the dips and thicknesses of those lava packages led us to estimate that $\sim 10 \text{ km}^3$ of volume was lost in collapses between 300 and 100 ka, \sim 15 km³ between 200 and 100 ka, and \sim 5 km³ from 100 to 18 ka (Figs. 2 and 3). The growth curve of the cone is steeper when the volume from caldera collapses is considered (Fig. 11).

The very slow growth rate between 100 and 18 ka may reflect: (1) the limited number of dates and a sampling bias between 80 and 26 ka; (2) elevated erosion rates during the LGM between 45 and 18 ka, which is supported by the ice-lava interaction features in the outcrops of unit Arb (Fig. 8); or (3) suppression of volcanism under the increasing load of the Patagonian Ice Sheet. We note that similarly slow rates of cone growth during this same period of time are observed at Puyehue (Singer et al., 2008) and Calbuco volcanoes (Mixon et al., 2021). Moreover, Ruapehu volcano in New Zealand also displays a lacuna between 80 and 50 ka (Conway et al., 2016; Pure et al., 2020), which may bolster an interpretation that instead of sampling bias, subdued eruptions due to ice loading during the global MIS 4 between 71 and 57 ka best explain these records (Fig. 11). Integration of the tephra volume estimated by Rawson et al. (2015) with estimated lava thicknesses indicates that the cone grew rapidly by \sim 6 km³ between 18 and 12 ka and 4 km³ between 12 and 8 ka. Notably, a "headless" dacitic lava truncated at the caldera rim and previously interpreted to be younger than 60 ka (Moreno and Lara, 2007; Table S5) is dated at 16.6 ± 2.4 ka. Thus, the caldera collapsed during the past 16 k.y. (Fig. 3). We propose that eruption of the \sim 5.3 km³ of Neltume rhyolitic tephra at 11.5 ka led to collapse of the 3.5-km-wide caldera, which was filled with lavas from the Arb unit. The MC2 tephra that erupted at ca. 13.5 ka-now thought to be more extensive than previously reported (Alloway et al., 2022)—could have also produced the collapse. Between 6 and 2 ka, eruptions are marked by the Adec, Hac, and Adm units, which together comprise $\sim 1.0 \text{ km}^3$ and build up the current Mocho cone and minor eruptive centers in its flanks. Finally, the 1.6 ka Enco ignimbrite (1.7 km³), 1.3 ka Hua-Hum tephra (0.4 km³; Rawson et al., 2015), the Hr unit, and the recent eruptions of the Adm unit (0.5 km³) led to a Late Holocene growth rate of $\sim 1.6 \text{ km}^3/\text{k.y.}$

IMPLICATIONS AND CONCLUSIONS

An apparent uptick in the volume of tephra that erupted immediately following deglaciations has led to the hypothesis that glacial retreat played a role (Huybers and Langmuir, 2009; Watt et al., 2013; Kutterolf et al., 2019). Moreover, based on the post-LGM tephra record, it has been inferred that, with respect to both magma composition and eruptive rates, Mocho-Choshuenco exhibits a strong response to rapid unloading of the Patagonian Ice Sheet (Rawson et al., 2016a). Our high-resolution chronostratigraphy spanning the past 50 k.y. (Fig. 10B), and time-volume constraints (Fig. 11), which are linked to rock compositions, now permit a more thorough comparison of Mocho-Choshuenco with neighboring volcanoes to evaluate impacts of glacial loading and unloading on the underlying magma plumbing systems during a full cycle of growth and retreat of the Patagonian Ice Sheet.

The pre-LGM lava record proves invaluable in revealing a compartmentalized plumbing system that operates during a complete cycle of glacial growth and decay. We highlight four key findings from the behavior of the Mocho-Choshuenco magma plumbing system: (1) the generation of both incompatible elementrich and element-poor reservoirs of eruptive magma; (2) a strong shift from basaltic andesitic to silicic magmas erupting beginning at 18 ka, when the Patagonian Ice Sheet began to retreat rapidly; (3) a notable increase in the eruptive rate immediately after ice retreat; and (4) the return to basaltic andesitic to dacitic eruptions during the Holocene as the volcano became icefree. We suggest that the increase in surface load due to the growth of the Patagonian Ice Sheet

beginning at 45 ka increased lithostatic stress in the mid-crust that impeded the ascent and eruption of magma from an incompatible elementpoor magma reservoir after 45 ka (Figs. 12A and 12B). The paucity of lavas on Calbuco volcano (Fig. 1) between 55 ka and 30 ka parallels our findings on Mocho-Choshuenco and supports regional ice loading as a mechanism for reducing volcanism (Fig. 11; Mixon et al., 2021). Coevally, a reservoir of incompatible element-rich magma grew, as magma ponded and heated deep to middle crustal rocks, thereby enhancing assimilation (Fig. 12B). Small quantities of basaltic andesitic magma stored within this reservoir began to erupt at ca. 26 ka and continued until 18 ka (Fig. 12C). The rapid decrease in surface loading as the Patagonian Ice Sheet began to retreat at 18 ka reduced the vertical stress on this magma reservoir and enabled dike propagation (Fig. 12D; Jellinek et al., 2004) that fueled the explosive eruption of Neltume rhyolite, and caldera collapse at 11.5 ka (Fig. 12E). Basaltic andesitic lavas emplaced at 12 ka bypassed the emptied silicic magma reservoir to erupt, which indicates that some mafic magmas may pond, whereas others ascend unimpeded, likely due to differences in density, viscosity, and H₂O content (Fig. 12E). Once the long-stored silicic magma erupted from the upper portion of this magma reservoir, mafic magmas from deeper parts of the transcrustal plumbing system ascended and began to dominate the eruptive volumes (Fig. 12F, Grupo Fui and Hac). After 2.9 ka, eruptions are of mainly intermediate to silicic compositions (60.1–65.0 wt% SiO₂), with some minor basaltic andesites (52.7–55.6 wt% SiO₂) and minor eruptive centers (Hr unit), which suggests that by this time, the upper portion of the magma plumbing system had cooled, crystallized, and produced intermediate melts and magmas similar to those that erupted prior to the local LGM glaciation.

Our findings from the pre-Holocene effusive eruptions of Mocho Choshuenco expand upon those of Rawson et al. (2016a) and allow us to consider the behavior of the magma plumbing system before, during, and after the LGM. For instance, an increase of an order of magnitude in growth rate is observed immediately following the penultimate glaciation (Fig. 11; MIS 6 at 190-135 ka). Rawson et al. (2016a) suggest that an ~5 k.y. lag between deglaciation and eruption of the Neltume rhyolite at 11.5 ka reflects a slow viscoelastic response to unloading of the Patagonian Ice Sheet. Our observations indicate that voluminous dacitic lavas erupted at 18 ka during or immediately following Patagonian Ice Sheet retreat. Thus, there may be little, if any, time gap between ice retreat and silicic eruption

(Fig. 10B). Moreover, the magma plumbing system is compartmentalized into discrete reservoirs that allow some mafic magmas to erupt at 12 ka synchronously with or in close temporal proximity to the Neltume rhyolite. Moreover, eruption rates increased from <0.02 km³/k.y. during the LGM to 0.2 km3/k.y. when deglaciation began (18-12 ka) to a high of 1.7 km³/k.y. as the volcano became free of ice between 12 and 8 ka (Fig. 11). Other nearby volcanoes in the Andean Southern Volcanic Zone that were likely impacted by the growth and retreat of the Patagonian Ice Sheet (Antuco-Sierra Velluda, Puyehue, and Calbuco) show similar cone growth but with a sharp increase in eruptive rates immediately following deglaciation at 18 ka (Fig. 11). This difference occurs because, despite dacites erupting when ice retreats, the first large post-LGM eruption at Mocho-Choshuenco was at 11.5 ka. If a significant volume of the 13.5 ka MC2 tephra is confirmed with further mapping of its thickness and distribution (Alloway et al., 2022), the post-16 ka growth rate may require upward revision.

Puyehue and Mocho-Choshuenco volcanoes share the rapid increase in growth rate after the penultimate glaciation and LGM (Fig. 11), and also the abrupt shifts in compositions during and following glaciation. For instance, Puyehue volcano (Fig. 1) is predominantly basaltic andesitic to andesitic from 350 to 20 ka but abruptly shifts to erupt both basalts and rhyolite after 20 ka (Fig. 10C; Singer et al., 2008). Although Mocho-Choshuenco volcano is not bimodal, both volcanoes show an increase in silicic eruptions and cone growth rate coeval with ice retreat (Figs. 10 and 11). We suggest that the intracrustal stress drop associated with rapid deglaciation destabilizes arc front magma plumbing systems to facilitate highly explosive silicic eruptions as at Mocho-Choshuenco and Puyehue. Osorno is a dominantly basaltic andesitic volcano that lies 65 km south of Puyehue (Fig. 1), and it also has only erupted dacites in post-LGM time between ca. 11 and 8 ka (Moreno et al., 2010; Bechon et al., 2022).

Other Andean Southern Volcanic Zone volcanoes have responded differently to the growth and retreat of the Patagonian Ice Sheet. For example, the Antuco–Sierra Velluda Volcanic Complex shifts from erupting a spectrum of basaltic to andesitic magma between ca. 100 and 20 ka to erupting mainly MgOrich basalt after the LGM (Fig. 10C; Martínez et al., 2018). Villarrica, ~50 km north of Mocho-Choshuenco and Calbuco volcanoes (Fig. 1), experienced large explosive eruptions following glaciation, the Licán ignimbrite, and dome collapse at 16 ka, respectively. However, Calbuco volcano is monotonously

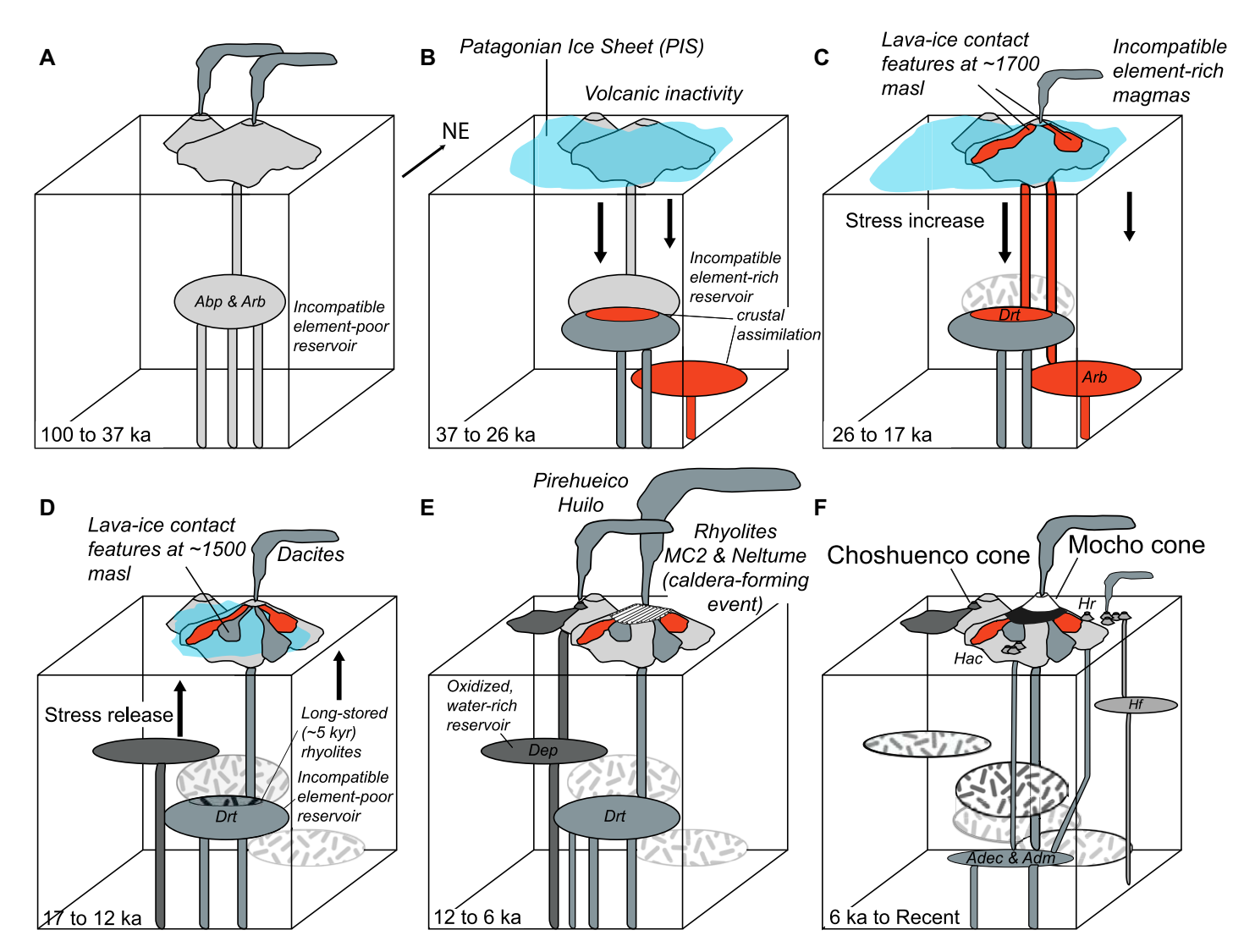


Figure 12. Schematic evolution of the upper portion of the magma plumbing system beneath Mocho-Choshuenco (not to scale). (A) Eruption of incompatible element-poor magmas from a common reservoir with different mantle sources that generated the old portion of the Mocho and Choshuenco composite cones: the Mocho-Choshuenco Ancestral (*Mca*) unit, Andesitas basálticas de Punahue (*Abp*) unit, and part of the Andesitas basálticas del Río Blanco (*Arb*) unit. (B) Growth of the Patagonian Ice Sheet at ca. 40 ka inhibited eruptions due to increasing lithostatic stress, limiting dike ascent and instead promoting enhanced crustal assimilation by basalt in the lower crust. (C) Incompatible element-rich basaltic andesites (*Arb* unit, in red), followed by incompatible element-rich dacites (Dacitas y Andesitas del Río Truful unit, *Drt*, in red) erupted from the reservoir; a separate incompatible element-poor reservoir builds up, from which eruptions are mainly (D) dacites with lava-ice contact features and (E) caldera-forming rhyolites (MC2 and Neltume between 13.5 and 11.5 ka). Eruptions forming the modern Choshuenco cone are from an oxidized, water-rich magma reservoir. (F) Basaltic magma ascends throughout the roots of now emptied and crystallized reservoirs to generate minor eruptive centers on the flanks of two Mocho-Choshuenco units, Alto Caunahue (*Hac*) and Ranquil (*Hr*), and Grupo Fui. Schematic depths of the reservoirs are based on thermobarometric estimates for magmas erupted at Mocho-Choshuenco (Moreno-Yaeger et al., 2022) that are consistent with other volcanoes in the Andean Southern Volcanic Zone (e.g., Lohmar et al., 2012; Castro et al., 2013; Brahm et al., 2018; Morgado et al., 2019; Arzilli et al., 2019; Vander Auwera et al., 2021; Boschetty et al., 2022; Morgan et al., 2024), which suggests magma storage depths of between 4 and 12 km. *Dep*—Andesitas del Estero Pirinel unit.

andesitic throughout its entire volcanic history (Fig. 10C; Mixon et al., 2021), and Villarrica has erupted only basaltic andesitic to andesitic magma following the local LGM (Moreno and Clavero, 2006; Lohmar et al., 2012). Some have suggested that mantle melt production and flux into the lower crust modulates how

transcrustal magma plumbing systems operate in the Cascade arc (Till et al., 2019). Higher mantle melt flux into the base of a plumbing system—as at Calbuco and Villarrica volcanoes—could prevent cooling, stalling, and differentiation to produce significant amounts of silicic melt (Mixon et al., 2021).

A more nuanced examination of the impact of ice loading and unloading on the plumbing systems beneath these volcanoes awaits application of phase equilibria constraints, using both natural mineral and melt compositions, in tandem with thermodynamic modeling (e.g., Bechon et al., 2022; DeSilva et al., 2023). Ther-

mobarometry coupled with numerical modeling of surface loading and unloading of the Patagonian Ice Sheet (e.g., Cuzzone et al., 2024) may provide further insights into how magma storage conditions and eruptive activity might have been influenced by ice sheet growth and retreat during the past 50 k.y.

ACKNOWLEDGMENTS

We thank Chris Conway and an anonymous reviewer for their constructive reviews, and science editor Mihai Ducea and associate editor Gary Michelfelder. Additionally, we thank Bryan Wathen, Bil Schneider, Drae Rogers, Alec Bauldry, and Tori Nelson for lab assistance, and Shaun Marcott, Sally Stevens, Matias Romero, Franco Vera, Matt Foote, and Monica Cummings for field support. Fieldwork was possible thanks to Corporación Nacional Forestal (CONAF), Fundación Huilo-Huilo, rangers of the Reserva Nacional Mocho-Choshuenco and Reserva Biológica Huilo-Huilo, and helicopter support from Barraco Air (Jaime Fernández and pilot Francisco Esquivel). Searching of local newspapers was possible thanks to the Biblioteca Nacional de Chile. This work was supported by a Chilean ANID grant (no. 722200330; Chilean Agency for Research and Development) to P. Moreno-Yaeger; a Vilas Professorship award from the University of Wisconsin-Madison to B.S. Singer; and National Science Foundation grants to B.S. Singer (no. EAR-212570) and B.R. Edwards (no. EAR-2121537).

REFERENCES CITED

- Alloway, B.V., Pearce, N.J., Moreno, P.I., Villarosa, G., Jara, I.A., Henríquez, C.A., Sagredo, E.A., Ryan, M.T., and Outes, V., 2022, Refinement of the tephrostratigraphy straddling the northern Patagonian Andes (40–41°S): New tephra markers, reconciling different archives and ascertaining the timing of piedmont deglaciation: Journal of Quaternary Science, v. 37, no. 3, p. 441–477, https://doi.org/10.1002/jqs.3389.
- Andersen, N.L., Singer, B.S., Jicha, B.R., Beard, B.L., Johnson, C.M., and Licciardi, J.M., 2017, Pleistocene to Holocene growth of a large upper crustal rhyolitic magma reservoir beneath the active Laguna del Maule Volcanic Field, central Chile: Journal of Petrology, v. 58, p. 85–114, https://doi.org/10.1093/petrology/egx006.
- Arzilli, F., Morgavi, D., Petrelli, M., Polacci, M., Burton, M., Di Genova, D., Spina, L., La Spina, G., Hartley, M.E., Romero, J.E., Fellowes, J., Diaz-Alvarado, J., and Perugini, D., 2019, The unexpected explosive sub-Plinian eruption of Calbuco (22–23 April 2015; southern Chile): Triggering mechanism implications: Journal of Volcanology and Geothermal Research, v. 378, p. 35–50, https://doi.org/10.1016/j.jvolgeores.2019.04.006.
- ASF DAAC (Alaska Satellite Facility Distributed Active Archive Center), 2022, _Radiometric_Terrain_Corrected_hi_res: ALOS PALSAR: https://doi.org/10.5067/JBYK3J6HFSVF (accessed September 2022).
- Avouris, D.M., Carn, S.A., and Waite, G.P., 2017, Triggering of volcanic degassing by large earthquakes: Geology, v. 45, p. 715–718, https://doi.org/10.1130/G39074.1.
- Bechon, T., Billon, M., Namur, O., Bolle, O., Fugmann, P., Foucart, H., Devidal, J.L., Delmelle, N., and Vander Auwera, J., 2022, Petrology of the magmatic system beneath Osorno volcano (Central Southern Volcanic Zone, Chile): Lithos, v. 426–427, https://doi.org/10 .1016/j.lithos.2022.106777.
- Belousov, A., Belousova, M., Hoblitt, R., and Patia, H., 2020, The 1951 eruption of Mount Lamington, Papua New Guinea: Devastating directed blast triggered by small-scale edifice failure: Journal of Volcanology and Geothermal Research, v. 401, https://doi.org/10.1016/j.jvolgeores.2020.106947.

- Boschetty, F.O., Ferguson, D.J., Cortés, J.A., Morgado, E., Ebmeier, S.K., Morgan, D.J., Romero, J.E., and Silva Parejas, C., 2022, Insights into magma storage beneath a frequently eruptic arc volcano (Villarrica, Chile) from supervised machine learning analysis of mineral compositions: Geochemistry, Geophysics, Geosystems, v. 23, https://doi.org/10.1029/2022GC010333.
- Brahm, R., Parada, M.A., Morgado, E., Contreras, C., and McGee, L.E., 2018, Origin of Holocene trachyte lavas of Quetrupillán volcanic complex, Chile: Examples of residual melts in a rejuvenated crystalline mush reservoir: Journal of Volcanology and Geothermal Research, v. 357, p. 163–176, https://doi.org/10.1016/j.jvolgeores .2018.04.020.
- Caricchi, L., Townsend, M., Rivalta, E., and Namiki, A., 2021, The build-up and triggers of volcanic eruptions: Nature Reviews Earth & Environment, v. 2, p. 458–476, https://doi.org/10.1038/s43017-021-00174-8.
- Cashman, K.V., Sparks, R.S.J., and Blundy, J.D., 2017, Vertically extensive and unstable magmatic systems: A unified view of igneous processes: Science, v. 355, https://doi.org/10.1126/science.aag3055.
- Castro, J.M., Schipper, C.I., Mueller, S.P., Militzer, A.S., Amigo, A., Silva Parejas, C., and Dorrit, J., 2013, Storage and eruption of near-liquidus rhyolite magma at Cordón Caulle, Chile: Bulletin of Volcanology, v. 75, https://doi.org/10.1007/s00445-013-0702-9.
- Cembrano, J., and Lara, L., 2009, The link between volcanism and tectonics in the southern volcanic zone of the Chilean Andes: A review: Tectonophysics, v. 471, p. 96–113, https://doi.org/10.1016/j.tecto.2009.02.038.
- "Choshuenco: Oficina del Registro Civil," 1955, September: La Voz de Panguipulli, p. 5.
- Conrey, R.M., Bailey, D.G., Singer, J.W., Wagoner, L.J., Parfitt, B., Hay, J., Keh, O., Chang, Z., and Huang, S., 2023, Combined use of multiple external and internal standards in LA-ICPMS analysis of bulk geological samples using lithium borate fused glass: Geochemistry Exploration Environment Analysis, v. 23, https://doi .org/10.1144/geochem2023-001.
- Conway, C.E., Townsend, D.B., Leonard, G.S., Wilson, C.J.N., Calvert, A.T., and Gamble, J.A., 2015, Lava-ice interaction on a large composite volcano: A case study from Ruapehu, New Zealand: Bulletin of Volcanology, v. 77, https://doi.org/10.1007/s00445-015-0906-2.
- Conway, C.E., Leonard, G.S., Townsend, D.B., Calvert, A.T., Wilson, C.J.N., Gamble, J.A., and Eaves, S.R., 2016, A high resolution ⁴⁰Ar/³⁹Ar lava chronology and edifice construction history for Ruapehu volcano, New Zealand: Journal of Volcanology and Geothermal Research, v. 327, p. 152–179, https://doi.org/10.1016/j.jvolgeores 2016.07.006.
- Conway, C.E., Gamble, J.A., Wilson, C.J.N., Leonard, G.S., Townsend, D.B., and Calvert, A.T., 2018, New petrological, geochemical and geochronological perspectives on andesite-dacite magma genesis at Ruapehu volcano, New Zealand: The American Mineralogist, v. 103, p. 565–581, https://doi.org/10.2138/am-2018-6199.
- Conway, C.E., Pure, L.R., and Ishizuka, O., 2023, An assessment of potential causal links between deglaciation and eruption rates at arc volcanoes: Frontiers of Earth Science, v. 11, p. 1–32, https://doi.org/10.3389/feart .2023.1082342.
- Cuzzone, J., Romero, M., and Marcott, S.A., 2024, Modeling the timing of Patagonian Ice Sheet retreat in the Chilean Lake District from 22–10 ka: The Cryosphere, v. 18, p. 1381–1398, https://doi.org/10.5194/tc-18-1381-2024.
- Davidson, J., Turner, S., Handley, H., Macpherson, C., and Dosseto, A., 2007, An amphibole "sponge" in arc crust: Geology, v. 35, p. 787–790, https://doi.org/10.1130/G23637A.1.
- Davies, B.J., et al., 2020, The evolution of the Patagonian Ice Sheet from 35 ka to the present day (PATICE): Earth-Science Reviews, v. 204, https://doi.org/10.1016/j.earscirev.2020.103152.
- DeMets, C., Gordon, R.G., and Argus, D.F., 2010, Geologically current plate motions: Geophysical Journal International, v. 181, p. 1–80, https://doi.org/10.1111/j.1365-246X.2009.04491.x.
- Denton, G.H., Heusser, C.J., Lowel, T.V., Moreno, P.I., Andersen, B.G., Heusser, L.E., Schlüchter, C., and

- Marchant, D.R., 1999, Interhemispheric linkage of paleoclimate during the last glaciation: Geografiska Annaler, v. 81, no. 2, p. 107–153, https://doi.org/10.1111/1468-0459.00055.
- Denton, G.H., Putnam, A.E., Russell, J.L., Barrell, D.J.A., Schaefer, J.M., Kaplan, M.R., and Strand, P.D., 2021, The Zealandia Switch: Ice age climate shifts viewed from Southern Hemisphere moraines: Quaternary Science Reviews, v. 257, https://doi.org/10.1016/j .quascirev.2020.106771.
- DeSilva, C.M., Singer, B.S., Alloway, B., and Moreno-Yaeger, P., 2023, Origin of the compositionally zoned Paso Puyehue Tephra, Antillanca Volcanic Complex, Chile: Journal of Volcanology and Geothermal Research, v. 444, https:// doi.org/10.1016/j.jvolgcores.2023.107943.
- Di Biase, F., 1976, Geología del Grupo Volcánico Mocho-Choshuenco, Provincia de Valdivia, Chile: Congreso Geológico Chileno, v. 1, Santiago, Chile, Actas 1, p. 1–17.
- Donovan, J.J., Singer, J.W., and Armstrong, J.T., 2016, A new EPMA method for trace element analysis in simple matrices: The American Mineralogist, v. 101, p. 1839–1853, https://doi.org/10.2138/am-2016-5628.
- Echegaray, J., 2004, Evolución geológica y geoquímica del Centro Volcánico Mocho-Choshuenco, Andes del Sur [Master's thesis]: Santiago, Chile, University of Chile, 121 p.
- Edwards, B., Kochtitzky, W., and Battersby, S., 2020, Global mapping of future glaciovolcanism: Global and Planetary Change, v. 195, https://doi.org/10.1016/j.gloplacha .2020.103356.
- Edwards, B.R., and Russell, J.K., 2002, Glacial influences on morphology and eruptive products of Hoodo Mountain volcano, Canada, in Smellie, J.L., and Chapman, M.G., eds., Volcano-Ice Interaction on Earth and Mars: Geological Society, London, Special Publication 202, p. 179–194
- Edwards, B.R., Russell, J.K., and Anderson, R.G., 2002, Subglacial, phonolitic volcanism at Hoodoo Mountain volcano, northwestern Canadian Cordillera: Bulletin of Volcanology, v. 64, p. 254–272, https://doi.org/10.1007 /s00445-002-0202-9.
- Edwards, B.R., Gudmundsson, M.T., and Russell, J.K., 2015, Chapter 20—Glaciovolcanism, in Sigurdsson, H., eds., The Encyclopedia of Volcanoes (second edition): Academic Press, p. 377–393, https://doi.org/10.1016/B978-0-12-385938-9.00020-1.
- Fenton, C.R., and Niedermann, S., 2014, Surface exposure dating of young basalts (1–200 ka) in the San Francisco volcanic field (Arizona, USA) using cosmogenic ³He and ²¹Ne: Quaternary Geochronology, v. 19, p. 87–105, https://doi.org/10.1016/j.quageo.2012.10.003.
- Ferrier, K.L., Perron, J.T., Mukhopadhyay, S., Rosener, M., Stock, J.D., Huppert, K.L., and Slosberg, M., 2013, Covariation of climate and long-term erosion rates across a steep rainfall gradient on the Hawaiian island of Kaua'i: Geological Society of America Bulletin, v. 125, p. 1146–1163, https://doi.org/10.1130/B30726.1.
- Fontijn, K., Lachowycz, S.M., Rawson, H., Pyle, D.M., Mather, T.A., Naranjo, J.A., and Moreno-Roa, H., 2014, Late Quaternary tephrostratigraphy of southern Chile and Argentina: Quaternary Science Reviews, v. 89, p. 70–84, https://doi.org/10.1016/j.quascirev.2014.02.007.
- Gardeweg, M., 2010, Geología y Peligros Volcánicos, Complejo Volcánico Mocho-Choshuenco y Grupo Volcánico Fui—Región de Los Ríos: Impacto en la Central Neltume: Aurum Consultores, 28 p.
- Gardeweg, M., and Sellés, D., 2012, Los volcanes Chanchán y el Grupo Volcánico Fui: Volcanes monogenéticos al norte del CV Mocho-Choshuenco, Región de los Ríos, sur de Chile: Congreso Geológico Chileno, v. 13, p. 591–593.
- Glasser, N.F., Jansson, K.N., Harrison, S., and Kleman, J., 2008, The glacial geomorphology and Pleistocene history of South America between 38°S and 56°S: Quaternary Science Reviews, v. 27, p. 365–390, https://doi.org/ /10.1016/j.quascirev.2007.11.011.
- Global Volcanism Program, 2023, Mocho-Choshuenco (375130), in Venzke, E., comp., Volcanoes of the World [database], v. 5.0.4, 1 November 2022: Smithsonian Institution, https://volcano.si.edu/volcano.cfm?vn=357130 (accessed May 2023).

- Göll, F., 1904, Die erdberen Chiles: München, Theodor Ackermann, 137 p.
- González-Ferrán, O., 1995, Volcanes de Chile: Instituto Geográfico Militar, 640 p.
- Gouhier, M., and Paris, R., 2019, SO₂ and tephra emissions during the December 22, 2018 Anak Krakatau flankcollapse eruption: Volcanica, v. 2, p. 91–103, https:// doi.org/10.30909/vol.02.02.91103.
- Harris, M.A., Russell, J.K., Wilson, A., and Jicha, B., 2023, A 500 ka record of volcanism and paleoenvironment in the northern Garibaldi Volcanic Belt, British Columbia: Canadian Journal of Earth Sciences, v. 60, no. 4, p. 401–421, https://doi.org/10.1139/cjes-2022-0101.
- Hickey-Vargas, R., Holbik, S., Tormey, D., Frey, F.A., and Moreno Roa, H., 2016, Basaltic rocks from the Andean Southern Volcanic Zone: Insights from the comparison of along-strike and small-scale geochemical variations and their sources: Lithos, v. 258–259, p. 115–132, https://doi.org/10.1016/j.lithos.2016.04.014.
- Hill, D.P., Pollitz, F., and Newhall, C., 2002, Earthquake-volcano interactions: Physics Today, v. 55, no. 11, p. 41–47, https://doi.org/10.1063/1.1535006.
- Hora, J.M., Singer, B.S., and Wörner, G., 2007, Volcano evolution and eruptive flux on the thick crust of the Andean Central Volcanic Zone: 40Art/39Ar constraints from Volcán Parinacota, Chile: Geological Society of America Bulletin, v. 119, p. 343–362, https://doi.org /10.1130/B25954.1.
- Huber, C., Townsend, M., Degruyter, W., and Bachmann, O., 2019, Optimal depth of subvolcanic magma chamber growth controlled by volatiles and crust rheology: Nature Geoscience, v. 12, p. 762–768, https://doi.org/10 .1038/s41561-019-0415-6.
- Huybers, P., and Langmuir, C., 2009, Feedback between deglaciation, volcanism, and atmospheric CO₂: Earth and Planetary Science Letters, v. 286, p. 479–491, https://doi.org/10.1016/j.epsl.2009.07.014.
- Jarosewich, E., Nelen, J.A., and Norberg, J.A., 1980, Reference samples for electron microprobe analysis: Geostandards and Geoanalytical Research, v. 4, p. 43–47, https://doi.org/10.1111/j.1751-908X.1980.tb00273.x.
- Jellinek, A.M., Manga, M., and Saar, M.O., 2004, Did melting glaciers cause volcanic eruptions in eastern California?: Probing the mechanics of dike formation: Journal of Geophysical Research: Solid Earth, v. 109, https://doi.org/10.1029/2004JB002978.
- Jicha, B.R., Singer, B.S., and Sobol, P., 2016, Re-evaluation of the ages of ⁴⁰Ar/³⁹Ar sanidine standards and supereruptions in the western U.S. using a Noblesse multicollector mass spectrometer: Chemical Geology, v. 431, p. 54–66, https://doi.org/10.1016/j.chemgeo.2016.03 .024.
- Jicha, B.R., Garcia, M.O., and Lormand, C., 2023, A possible sea-level fall trigger for the youngest rejuvenated volcanism in Hawai'i: Geological Society of America Bulletin, v. 135, p. 2478–2485, https://doi.org/10.1130/B36615.1.
- Jochum, K.P., et al., 2006, MPDI-DING reference glasses for in situ microanalysis: New reference values for element concentrations and isotope ratios: Geochemistry, Geophysics, Geosystems, v. 7, p. 5–27, https://doi.org /10.1029/2005GC001060.
- Klug, J.D., Ramirez, A., Singer, B.S., Jicha, B.R., Mixon, E.M., and Martínez, P., 2022, Intercalibration of the Servicio Nacional de Geología y Minería (SER-NAGEOMIN), Chile and WiscAr ⁴⁰Ar/³⁹Ar laboratories for Quaternary dating: Quaternary Geochronology, v. 72, https://doi.org/10.1016/j.quageo.2022.101354.
- Kurz, M.D., 1986, In situ production of terrestrial cosmogenic helium and some applications to geochronology: Geochimica et Cosmochimica Acta, v. 50, p. 2855–2862, https://doi.org/10.1016/0016-7037(86)90232-2.
- Kurz, M.D., Rowland, S.K., Curtice, J., Saal, A.E., and Naumann, T., 2014, Chapter 4—Eruption rates for Fernandina Volcano, in Harpp, K.S., Mittelstaedt, E., d'Ozouville, N., and Graham, D.W., eds., The Galápagos: A Natural Laboratory For the Earth Sciences: American Geophysical Union, Geophysical Monograph 204, p. 41–54, https://doi.org/10.1002 /9781118852538.ch4.
- Kutterolf, S., Schindlbeck, J.C., Jegen, M., Freundt, A., and Straub, S.M., 2019, Milankovitch frequencies in tephra

- records at volcanic arcs: The relation of kyr-scale cyclic variations in volcanism to global climate changes: Quaternary Science Reviews, v. 204, p. 1–16, https://doi.org/10.1016/j.quascirev.2018.11.004.
- Lal, D., 1991, Cosmic ray labeling of erosion surfaces: In situ nuclide production rates and erosion models: Earth and Planetary Science Letters, v. 104, p. 424–439, https://doi.org/10.1016/0012-821X(91)90220-C.
- Lee, J.-Y., Marti, K., Severinghaus, J.P., Kawamura, K., Yoo, H.-S., Lee, J.B., and Kim, J.S., 2006, A redetermination of the isotopic abundance of atmospheric Ar: Geochimica et Cosmochimica Acta, v. 70, p. 4507–4512, https://doi.org/10.1016/j.gca.2006.06.1563.
- Lescinsky, D.T., and Fink, J.H., 1998, Ridge-forming, ice-bounded lava flows at Mount Rainier, Washington: Geology, v. 26, p. 351–354, https://doi.org/10.1130/0091-7613(1998)026<0351:RFIBLF>2.3.CO;2.
- Lifton, N., Sato, T., and Dunai, T.J., 2014, Scaling in situ cosmogenic nuclide production rates using analytical approximations to atmospheric cosmic-ray fluxes: Earth and Planetary Science Letters, v. 386, p. 149–160, https://doi.org/10.1016/j.epsl.2013.10.052.
- Lisiecki, L.E., and Raymo, M.E., 2005, A Pliocene-Pleistocene stack of 57 globally distributed benthic 818O records: Paleoceanography, v. 20, https://doi.org/10.1029 /2004PA001071.
- Lohmar, S., Parada, M., Gutiérrez, F., Robin, C., and Gerbe, M.C., 2012, Mineralogical and numerical approaches to establish the pre-eruptive conditions of the mafic Licán Ignimbrite, Villarrica Volcano (Chilean Southern Andes): Journal of Volcanology and Geothermal Research, v. 235–236, p. 55–69, https://doi.org/10.1016/j .jvolgeores.2012.05.006.
- López-Escobar, L., Parada, M.A., Moreno, H., Frey, F.A., and Kempton, R.D., 1995, Calbuco Volcano and minor eruptive centers distributed along the Liquiñe-Ofqui Fault Zone, Chile (41° -42°S): Contrasting origin of andesitic and basaltic magma in the Southern Volcanic Zone of the Andes: Contributions to Mineralogy and Petrology, v. 119, p. 345–361, https://doi.org/10.1007 //BF00/286934.
- Mallea-Lillo, F., Parada, M.A., Morgado, E., Contreras, C., and Hübner, D., 2022, Contrasting sources and conditions of shallow magmatic reservoirs of the Fui Group small eruptive centers associated with the Liquiñe-Ofqui Fault Zone (Chilean Andes): Journal of South American Earth Sciences, v. 117, https://doi.org/10.1016/j.jsames.2022.103875.
- Manga, M., 2007, Did an earthquake trigger the May 2006 eruption of the Lusi Mud volcano?: Eos (Transactions, American Geophysical Union), v. 88, p. 201, https://doi.org/10.1029/2007E0180009.
- Martínez, P., Singer, B.S., Moreno Roa, H., and Jicha, B.R., 2018, Volcanologic and petrologic evolution of Antuco-Sierra Velluda, Southern Andes, Chile: Journal of Volcanology and Geothermal Research, v. 349, p. 392– 408, https://doi.org/10.1016/j.jvolgeores.2017.11.026.
- McGuire, W.J., 1996, Volcano instability: A review of contemporary themes, in McGuire, W.J., Jones, A.P., and Neuberg, J., eds., Volcano Instability on the Earth and Other Planets: Geological Society, London, Special Publication 110, p. 1–23, https://doi.org/10.1144/GSL.SP.1996.110.01.01.
- McMillan, N.J., Harmon, R.S., Moorbath, S., López-Escobar, L., and Strong, D.F., 1989, Crustal sources involved in continental arc magmatism: A case study of volcan Mocho-Choshuenco, southern Chile: Geology, v. 17, p. 1152–1156, https://doi.org/10.1130/0091-7613(1989)017<1152:CSIICA>2.3.CO;2.
- Min, K., Mundil, R., Renne, P.R., and Ludwig, K.R., 2000, A test for systematic errors in ⁴⁰Ar/³⁹Ar geochronology through comparison with U/Pb analysis of a 1.1-Ga rhyolite: Geochimica et Cosmochimica Acta, v. 64, p. 73–98, https://doi.org/10.1016/S0016-7037(99)00204-5.
- Mixon, E.E., Singer, B.S., Jicha, B.R., and Ramirez, A., 2021, Calbuco, a monotonous andestitic high-flux volcano in the Southern Andes, Chile: Journal of Volcanology and Geothermal Research, v. 416, https://doi.org/10 .1016/j.jvolgeores.2021.107279.
- Mixon, E.E., Jicha, B.R., Tootell, D., and Singer, B.S., 2022, Optimizing 40Ar/39Ar analyses using an IsotopX NGX-

- 600 mass spectrometer: Chemical Geology, v. 593, https://doi.org/10.1016/j.chemgeo.2022.120753.
- Moreno, P.I., Denton, G.H., Moreno, H., Lowell, T.V., Putnam, A.E., and Kaplan, M.R., 2015, Radiocarbon chronology of the last glacial maximum and its termination in northwestern Patagonia: Quaternary Science Reviews, v. 122, p. 233–249, https://doi.org/10.1016/j .quascirev.2015.05.027.
- Moreno, R.H., and Clavero, J., 2006, Geología del Volcán Villarrica, región de La Araucanía y de Los Lagos: Servicio Nacional de Geología y Minería, Carta Geológica de Chile, Serie Geología Básica, v. 98, 1 sheet, scale 1:50,000.
- Moreno, R.H., and Lara, P.L., 2007, Geología del Complejo Volcánico Mocho-Choshuenco, región de Los Ríos: Servicio Nacional de Geología y Minería, Carta Geológica de Chile, Serie Geología Básica, v. 107, 1 sheet, scale 1:50.000.
- Moreno, R.H., Lara, L., and Orozco, G., 2010, Geología del Volcán Osorno: Servicio Nacional de Geología y Minería, Carta Geológica de Chile, Serie Geología Básica, v. 126, 1 sheet, scale 1:50,000.
- Moreno-Yaeger, P., Singer, B.S., Jicha, B.R., Nachlas, W.O., Fustos-Toribio, I., and Vásquez-Antipán, D., 2022, Evolution of magma storage conditions spanning the last glacial-interglacial transition, Mocho-Choshuenco Volcanic Complex, Chile: Abstract V13A-02 presented at 2022 Fall Meeting, AGU, Chicago, USA.
- Morgado, E., Morgan, D.J., Castruccio, A., Ebmeier, S.K., Parada, M.-Á., Brahm, R., Harvey, J., Gutiérrez, F., and Walshaw, R., 2019, Old magma and a new, intrusive trigger: Using diffusion chronometry to understand the rapid-onset Calbuco eruption, April 2015 (Southern Chile): Contributions to Mineralogy and Petrology, v. 174, 61, https://doi.org/10.1007/s00410-019-1596-0.
- Morgan, C., Morgado, E., Parada, M.-Á., Brahm, R., and Mallea-Lillo, F., 2024, Two-stage evolution of a bimodal reservoir: The case of Holocene lavas of the Lanín volcano, Southern Volcanic Zone, Chile: Journal of South American Earth Sciences, v. 133, https://doi .org/10.1016/j.jsames.2023.104697.
- Murphy, M.A., and Salvador, A., eds., 1999, International Stratigraphic Guide—An abridged version: Episodes, v. 22, p. 255–271, https://doi.org/10.18814/epiiugs/1999/v22i4/002.
- NASA Shuttle Radar Topography Mission, 2013, Shuttle Radar Topography Mission (SRTM) Global, distributed by OpenTopography: https://doi.org/10.5069/G9445JDF (accessed June 2023).
- Oddsson, B., Gudmundsson, M., Edwards, B.R., Thordarson, T., Magnússon, E., and Sigurðsson, G., 2016, Subglacial lava propagation, ice melting and heat transfer during emplacement of an intermediate lava flow in the 2010 Eyjafjalljojull eruption: Bulletin of Volcanology, v. 78, 48, https://doi.org/10.1007/s00445-016-1041-4.
- Pallister, J.S., Hoblit, R.P., Crandell, D.R., and Mullineaux, D.R., 1992, Mount St. Helens a decade after the 1980 eruptions: Magmatic models, chemical cycles, and a revised hazards assessment: Bulletin of Volcanology, v. 54, p. 126–146, https://doi.org/10.1007/BF00278003.
- Parmelee, D.E., Kyle, P.R., Kurz, M.D., Marrero, S.M., and Phillips, F.M., 2015, A new Holocene eruptive history of Erebus volcano, Antarctica using cosmogenic ³He and ³⁶Cl exposure ages: Quaternary Geochronology, v. 30, p. 114–131, https://doi.org/10.1016/j.quageo .2015.09.001.
- Peltier, C., Kaplan, M.R., Birkel, S.D., Soteres, R.L., Sagredo, E.A., Aravena, J.C., Araos, J., Moreno, P.I., Scwartz, R., and Schaefer, J.M., 2021, The large MIS 4 and long MIS 2 glacier maxima on the southern tip of South America: Quaternary Science Reviews, v. 262, https://doi.org/10.1016/j.quascirev.2021.106858.
- Pérez-Flores, P., Cembrano, J., Sánchez-Alfaro, P., Veloso, E., Arancibia, G., and Roquer, T., 2016, Tectonics, magmatism and paleo-fluid distribution in a strike-slip setting: Insights from the northern termination of the Liquiñe-Ofqui fault System, Chile: Tectonophysics, v. 680, p. 192–210, https://doi.org/10.1016/j.tecto.2016.05.016.
- Petit-Breuilh, S.M.A., 2004, La Historia Eruptiva de los Volcanes Hispanoamericanos (Siglos XVI al XX), El Modelo Chileno: Serie Casa de los Volcanes, v. 8, Imprenta Beltrán, 431 p.

- Preece, K., Mark, D.F., Barclay, J., Cohen, B.E., Chamberlain, K.J., Jowitt, Cl., Vye-Brown, C., Brown, R.J., and Hamilton, S., 2018, Bridging the gap: ⁴⁰Ar/³⁹Ar dating of volcanic eruptions from the 'Age of Discovery': Geology, v. 46, p. 1035–1038, https://doi.org/10.1130/G45415.1.
- Pure, L.R., Leonard, G.S., Townsend, D.B., Wilson, C.J.N., Calvert, A.T., Cole, R.P., Conway, C.E., Gamble, J.A., and Smith, T.B., 2020, A high resolution 40Arf³⁹Ar lava chronology and edifice construction history for Tongariro volcano, New Zealand: Journal of Volcanology and Geothermal Research, v. 403, https://doi.org/10 .1016/j.jvolgeores.2020.106993.
- Rawson, H., Naranjo, J.A., Smith, V.C., Fontijn, K., Pyle, D.M., Mather, T.A., and Moreno, H., 2015, The frequency and magnitude of post-glacial explosive eruptions at Volcán Mocho-Choshuenco, southern Chile: Journal of Volcanology and Geothermal Research, v. 299, p. 103– 129, https://doi.org/10.1016/j.jvolgeores.2015.04.003.
- Rawson, H., Pyle, D.M., Mather, T.A., Smith, V.C., Fontijn, K., Lachowycz, S.M., and Naranjo, J.A., 2016a, The magmatic and eruptive response of arc volcanoes to deglaciation: Insights from southern Chile: Geology, v. 44, p. 251–254, https://doi.org/10.1130/G37504.1.
- Rawson, H., Keller, T., Fontijn, K., Pyle, D.M., Mather, T.A., Smith, V.C., and Naranjo, J.A., 2016b, Compositional variability in mafic arc magmas over short spatial and temporal scales: Evidence for the signature of mantle reactive melt channels: Earth and Planetary Science Letters, v. 456, p. 66–77, https://doi.org/10 .1016/j.epsl.2016.09.056.
- Rodríguez, C., Pérez, Y., Moreno, H., Clayton, J., Antinao, J., Duhart, P., and Martin, M., 1999, Área de Panguipulli-Riñihue: Región de Los Lagos: Servicio Nacional de Geología y Minería, Mapas Geológicos, v. 10, scale 1:100.000.
- Rollinson, H., and Pease, V., 2021, Using Geochemical Data to Understand Geological Processes (second edition): Cambridge University Press, 358 p., https://doi.org/10 .1017/9781108777834.
- Satow, C., Gudmundsson, A., Gertisser, R., Ramsey, C.B., Bazargan, M., Pyle, D.M., Wulf, S., Miles, A.J., and Hardiman, M., 2021, Eruptive activity of the Santorini Volcano controlled by sea-level rise and fall: Nature Geoscience, v. 14, p. 586–592, https://doi.org/10 .1038/s41561-021-00783-4.

- Sawi, T.M., and Manga, M., 2018, Revisiting short-term earthquake triggered volcanism: Bulletin of Volcanology, v. 80, 57, https://doi.org/10.1007/s00445-018-1232-2.
- Schaen, A., et al., 2021, Interpreting and reporting ⁴⁰Ar/³⁹Ar geochronologic data: Geological Society of America Bulletin, v. 133, p. 461–487, https://doi.org/10.1130/B35560.1.
- SERNAGEOMIN (Servicio Nacional de Geología y Minería), 2020, Complejo Volcánico Mocho-Choshuenco, Servicio Nacional de Geología y Minería: https:// rnvv.sernageomin.cl/complejo-volcanico-mocho -choshuenco/ (accessed March 2023).
- Singer, B.S., Jicha, B.R., Harper, M.A., Naranjo, J.A., Lara, L.E., and Moreno-Roa, H., 2008, Eruptive history, geochronology, and magmatic evolution of the Puyehue-Cordón Caulle volcanic complex, Chile: Geological Society of America Bulletin, v. 120, p. 599–618, https://doi.org/10.1130/B26276.1.
- Singer, B.S., Costa, F., Herrin, J.S., Hildreth, W., and Fierstein, J., 2016, The timing of compositionally-zoned magma reservoirs and mafic 'priming' weeks before the 1912 Novarupta-Katmai rhyolite eruption: Earth and Planetary Science Letters, v. 451, p. 125–137, https://doi.org/10.1016/j.epsl.2016.07.015.Sisson, T.W., and Grove, T.L., 1993, Temperatures and H₂0
- Sisson, T.W., and Grove, T.L., 1993, Temperatures and H₂0 contents of low-MgO high-alumina basalts: Contributions to Mineralogy and Petrology, v. 113, p. 167–184, https://doi.org/10.1007/BF00283226.
- Smellie, J.L., and Edwards, B.R., 2016, Glaciovolcanism on Earth and Mars, Products, Processes and Paleoenvironmental Significance: Cambridge University Press, 483 p., https://doi.org/10.1017/CBO97811 39764384.
- Somoza, R., 1998, Updated Nazca (Farallon)-South America relative motions during the last 40 My: Implications for mountain building in the central Andean region: Journal of South American Earth Sciences, v. 11, no. 3, p. 211– 215, https://doi.org/10.1016/S0895-9811(98)00012-1.
- Stone, J.O., 2000, Air pressure and cosmogenic isotope production: Journal of Geophysical Research: Solid Earth, v. 105, p. 23,753–23,759, https://doi.org/10.1029 /20001B900181
- Sun, S.-s., and McDonough, W.F., 1989, Chemical and isotopic systematics of oceanic basalts: Implications for mantle composition and processes, in Saunders, A.D., and Norry, M.J., eds., Magmatism in the Ocean Basins: Geological

- Society, London, Special Publication 42, p. 313–345, https://doi.org/10.1144/GSL.SP.1989.042.01.19.
- Till, C.B., Kent, A.J.R., Abers, G.A., Janiszewski, H.A., Gaherty, J.B., and Pitcher, B.W., 2019, The causes of spatiotemporal variations in erupted fluxes and compositions along a volcanic arc: Nature Communications, v. 10, no. 1, 1350, https://doi.org/10.1038/s41467-019-09113-0.
- Townsend, M., 2022, Linking surface deformation to thermal and mechanical magma chamber processes: Earth and Planetary Science Letters, v. 577, https://doi.org/10.1016/j.epsl.2021.117272.
- Townsend, M., and Huber, C., 2020, A critical magma chamber size for volcanic eruptions: Geology, v. 48, p. 431–435, https://doi.org/10.1130/G47045.1.
- "Una Erupción del Volcán Mocho ha causado daños materiales," 1937, June: Austral de Temuco, p. 20.
- Vander Auwera, J., Montalbano, S., Namur, O., Bechon, T., Schiano, P., Devidal, J.-L., and Bolle, O., 2021, The petrology of a hazardous volcano: Calbuco (Central Southern Volcanic Zone, Chile): Contributions to Mineralogy and Petrology, v. 176, 46, https://doi.org/10 .1007/s00410-021-01803-7.
- Vidal Gormaz, F., 1869, Esploración del río Calle-Calle, provincia de Valdivia, XXXII: Anales de la Universidad de Chile, p. 34–35.
- Watt, S.F.L., Pyle, D.M., and Mather, T.A., 2013, The volcanic response to deglaciation: Evidence from glaciated arcs and a reassessment of global eruption records: Earth-Science Reviews, v. 122, p. 77–102, https://doi.org/10.1016/j.earscirev.2013.03.007.
- Wijbrans, J., Schneider, B., Kuiper, K., Calvari, S., Branca, S., De Beni, E., Norini, G., Corsaro, R.A., and Miraglia, L., 2011, ⁴⁰Ar/³⁹Ar geochronology of Holocene basalts; examples from Stromboli, Italy: Quaternary Geochronology, v. 6, p. 223–232, https://doi.org/10.1016/j.quageo.2010.10.003.
- Yokoyama, I., 1988, Seismic energy releases from volcanoes: Bulletin of Volcanology, v. 50, p. 1–13, https://doi.org/10.1007/BF01047504.

SCIENCE EDITOR: MIHAI DUCEA ASSOCIATE EDITOR: GARY S. MICHELFELDER

Manuscript Received 18 December 2023 Revised Manuscript Received 26 March 2024 Manuscript Accepted 30 April 2024